MASARYKOVA UNIVERZITA
Přírodovědecká fakulta
Ústav teoretické fyziky a astrofyziky

Bakalářská práce

Brno 2026 Klára Švestková

MASARYKOVA
UNIVERZITA
PŘÍRODOVĚDECKÁ FAKULTA
ÚSTAV TEORETICKÉ FYZIKY A ASTROFYZIKY

Omezení počáteční hmotnostní funkce hvězd v Galaxii pomocí neutrin vyzařovaných červenými veleobry

Bakalářská práce

Klára Švestková

Vedoucí práce: Dr. rer. nat. Tereza Jeřábková **Brno 2026**

Bibliografický záznam

Autor:	Klára Švestková Přírodovědecká fakulta, Masarykova univerzita Ústav teoretické fyziky a astrofyziky
Název práce:	Omezení počáteční hmotnostní funkce hvězd v Galaxii pomocí neutrin vyzařovaných červenými veleobry
Studijní program:	Fyzika
Studijní obor:	Astrofyzika
Vedoucí práce:	Dr. rer. nat. Tereza Jeřábková
Akademický rok:	2025/2026
Počet stran:	IV + 44
Klíčová slova:	Červení veleobři; IMF; Neutrina; Hoření uhlíku

Bibliographic Entry

Author:	Klára Švestková Faculty of Science, Masaryk University Department of Theoretical Physics and Astrophysics
Title of Thesis:	Constraining the Stellar Initial Mass Function in the Milky Way Using Neutrinos from Red Supergiants
Degree Programme:	Physics
Field of Study:	Astrophysics
Supervisor:	Dr. rer. nat. Tereza Jeřábková
Academic Year:	2025/2026
Number of Pages:	IV + 44
Keywords:	Red Supergiants; IMF; Neutrino; carbon-burning

Abstrakt

Zkoumáme potenciál budoucích neutrinových detektorů pro rozlišení variací vysokohmotnostního sklonu počáteční hmotnostní funkce hvězd (IMF) pomocí neutrin emitovaných červenými veleobry v Mléčné dráze během fáze spalování uhlíku. Pomocí jednoduchých variant IMF, předpokladu rychlosti tvorby hvězd v Mléčné dráze a evolučních drah PARSEC odhadujeme okamžitý (snapshot) počet červených veleobrů spalujících uhlík, včetně očekávaného počtu v okolí Slunce (do 1 kpc). Následně načrtneme řádový převod od počtu zdrojů k neutrinovému toku a očekávaným detekčním rychlostem a posuzujeme podmínky, za nichž by vlastnosti detektoru (fiduciální hmotnost, energetický práh a potlačení pozadí) umožnily dosáhnout měřitelné citlivosti na IMF. Podrobná simulace odezvy detektoru a vlivu stochastického výskytu zdrojů jsou ponechány jako budoucí práce.

Abstract

We assess the feasibility of using future neutrino detectors to probe variations of the high-mass stellar initial mass function (IMF) by targeting neutrinos emitted by carbon-burning red supergiants in the Milky Way. Using simple IMF variants, a Milky Way star formation rate, and PARSEC stellar evolution tracks, we estimate the snapshot number of carbon-burning red supergiants, including the expected number within 1 kpc of the Sun. We then outline an order-of-magnitude scaling from source counts to neutrino flux and expected event rates, identifying the conditions under which detector properties (fiducial mass, energy threshold, and background control) might allow for measurable sensitivity to the IMF. Detailed detector-response simulations and the impact of stochastic source distribution are left as future work.

MASARYKOVA UNIVERZITA
PŘÍRODOVĚDECKÁ FAKULTA
KOTLÁŘSKÁ 2, 611 37 BRNO
IČ: 00216224
DIČ: CZ00216224

ZADÁNÍ BAKALÁŘSKÉ PRÁCE

Akademický rok: 2025/2026

Ústav:	Ústav teoretické fyziky a astrofyziky
Studentka:	Klára Švestková
Program:	Fyzika
Specializace:	Astrofyzika

Ředitel *ústavu* PřF MU Vám ve smyslu Studijního a zkušebního řádu MU určuje bakalářskou práci s názvem:

Název práce:	Omezení počáteční hmotnostní funkce hvězd v Galaxii pomocí neutrin vyzařovaných červenými veleobry
Název práce anglicky:	Constraining the Stellar Initial Mass Function in the Milky Way Using Neutrinos from Red Supergiants
Jazyk práce:	angličtina

Oficiální zadání:
To explore the feasibility of using MeV-range neutrinos emitted by carbon-burning red supergiants (RSGs) as a novel tool to constrain the high-mass end of the stellar initial mass function (IMF) in the Milky Way. The thesis will connect stellar evolution models, neutrino emission mechanisms, and detectability with the predicted RSG population under various IMF assumptions.

The stellar initial mass function (IMF) plays a central role in understanding the formation and evolution of galaxies, yet its precise shape-especially at the high-mass end-remains uncertain. This thesis investigates a novel approach to constrain the IMF by modeling neutrinos emitted from red supergiants (RSGs) during their carbon-burning phase. Based on recent studies of MeV-range neutrino production in post-main-sequence massive stars, the expected total neutrino flux from the Galactic population of RSGs will be estimated for different IMF prescriptions. The detectability of these neutrinos will be evaluated using current and next-generation underground detectors, such as Super-Kamiokande and Hyper-Kamiokande. The study will assess whether the differences in predicted event rates between IMF scenarios are large enough to be observable, and will discuss the potential of neutrino astronomy as an independent method to probe stellar populations in the Milky Way, complementing electromagnetic observations.

Vedoucí práce:	Dr. rer. nat. Tereza Jeřábková
Datum zadání práce:	25. 6. 2025
V Brně dne:	17. 4. 2026

Zadání bylo schváleno prostřednictvím IS MU.

Klára Švestková, 12. 8. 2025
Dr. rer. nat. Tereza Jeřábková, 24. 11. 2025
RNDr. Luboš Poláček, 11. 12. 2025

Poděkování

Na prvním místě bych ráda poděkovala své vedoucí, Dr. rer. nat. Tereze Jeřábkové, za ochotu a pomoc při každém kroku, za pomoc s pochopením nových informací z astrofyziky a při psaní této bakalářské práce.

Za podporu při studiu a ve všech mých rozhodnutích bych ráda poděkovala rodičům, díky kterým jsem tam, kde jsem, a jsou mou největší oporou.

Mé poděkování patří i mým prarodičům za jejich důvěru ve mne a mým zvířátkům za jejich psychickou podporu.

Dále bych ráda poděkovala i svým přátelům, se kterými jsem strávila spoustu hodin při studiu i mimo něj a díky kterým jsem na nic nebyla sama.

Prohlášení

Prohlašuji, že jsem svoji bakalářskou práci vypracovala samostatně pod vedením vedoucího práce s využitím informačních zdrojů, které jsou v práci citovány.

Brno 13. května 2026 .....

Klára Švestková

Contents

List of Figures

List of Tables

INTRODUCTION

Massive stars represent a fundamental component of galactic evolution, playing a disproportionate role in galactic feedback and chemical enrichment through ionizing radiation, stellar winds, and core-collapse supernovae. Given this influence, the distribution of newly formed stars, described by the stellar initial mass function (IMF) $\xi(m) = dN/dm$, remains one of the central sources of uncertainty in astrophysical models[1, 2, 3].

The importance of the IMF lies in its direct impact on the predicted population of massive stars and their subsequent feedback. However, the universality of the IMF with respect to physical parameters such as density or metallicity remains a subject of debate[4, 5, 6]. Neutrinos produced by stars provide a distinct and complementary probe of massive-star physics. In advanced burning stages, massive stars emit "thermal" neutrinos produced by weak interaction processes in the hot stellar core. Recently, [7] investigated the detectability of neutrinos from carbon-burning red supergiants (RSGs), focusing on future large-volume detectors. These carbon-burning RSG neutrinos are particularly interesting because they offer a potential early warning and the possibility of probing the final evolution of nearby stars before they reach the supernova stage.

Project overview

This thesis represents an initial step toward a method that seeks to estimate how variations in the IMF might affect the sensitivity of the neutrino signal within the Milky Way. The primary calculation of this work combines three key elements: simple IMF variants, stellar evolution models to estimate the duration of the relevant evolutionary phase, and a simplified spatial toy model of the Milky Way.

Concretely, the thesis aims to:

- Compare a standard (Kroupa-like) IMF to “top-heavy” and “top-light” variants and quantify the change in the expected number of massive stars.
- Estimate the snapshot population of carbon-burning RSGs in the Milky Way from the IMF, a Galactic star formation rate, and the carbon-burning phase duration.
- Estimate the expected number of such stars within a local volume (e.g. within 1 kpc of the Sun) using a simple Monte Carlo spatial model.
- Translate the resulting source counts into an order-of-magnitude neutrino flux and expected event-rate scaling for representative detector masses.

To maintain a focused analysis, certain aspects are considered outside the scope of this thesis. Detailed simulations of detector response and complex background modeling are reserved for future work, following the framework established in [7]. Furthermore, the Galactic star formation rate is assumed to be fixed throughout this analysis together with the adopted stellar evolution framework.

The detection of neutrinos from RSGs during the carbon-burning phase is a challenging task, as these neutrinos reach very low energies, typically around 0.6 MeV [7]. Therefore, neutrino-electron elastic scattering is assumed as the primary interaction channel in this work. As representative benchmarks for future measurements, detector complexes such as Hyper-Kamiokande [8], JUNO [9], or the SK-Gd concept [10] are considered. While these facilities represent the current state of the art, the faint signal from carbon-burning RSGs requires even lower energy thresholds and stronger background rejection than currently available. Future hypothetical concepts, such as hybrid detectors utilizing water-based liquid scintillators (WbLS), could resolve limitations such as directionality and eventually help assess the variability of the initial mass function [7].

1 THEORETICAL PART

1.1 Initial Mass Function

The Initial Mass Function (IMF) is a term used to describe the distribution of stellar masses, first determined by astrophysicist Edwin Salpeter in 1955. According to Salpeter [1], more massive stars form significantly less frequently than less massive stars, with their number decreasing with increasing mass according to a power law. The IMF determines the relative proportion of stars formed for a given mass at their birth; using it along with the Star Formation Rate (SFR), it is possible to derive other characteristics such as chemical production, luminosity, or the evolution of the stellar population over time.

In general, the IMF is written as

$$\xi(m) = \frac{dN}{dm}, \tag{1.1}$$

The initial mass function (IMF) $\xi(m)$ represents the number of stars formed per unit mass interval and is calculated in units of $M_{\odot}^{-1}$, defined over the mass range of 0.08–100 $M_{\odot}$.

In this work, the IMF is normalized such that the total mass of the stellar population is equal to $1\,M_{\odot}$ according to the relation 1.2

$$\int_{m_{\min}}^{m_{\max}} m\,\xi(m)\,dm = 1\,\mathrm{M}_{\odot} \tag{1.2}$$

In the simplest case, the IMF can be approximated by a power law $\xi(m) \propto m^{-\alpha}$, with $\alpha = 2.35$ [1]. However, recent research shows that a single power law is not entirely accurate across all mass scales. Currently, two standard modern parameterizations are widely used:

- Chabrier's log-normal distribution for low-mass stars combined with a power law for high-mass stars [3].
- Kroupa's broken power law, where the IMF is defined as [2]:

$$\alpha \approx 1.3 \quad \text{for} \quad m < 0.5\,M_{\odot} \tag{1.3}$$

and

$$\alpha \approx 2.3 \quad \text{for} \quad m > 0.5\,M_{\odot}. \tag{1.4}$$

This is provided by the multi-mass law, which is a more accurate description of the distribution of stellar mass [2, 11].

The break occurring in Kroupa's IMF theory around $0.5\,M_{\odot}$ is a critical point representing a change in the distribution of the number of formed stars. This transition aligns with observations from diverse environments; by accounting for the influence of binary systems and the dynamical evolution of star clusters, this functional form serves as a widely accepted empirical model. The existence of a break at this value suggests a dependence on the ambient density across the entire Galaxy [12].

For this reason, we worked with the Kroupa variant, which is most suitable for the Milky Way.

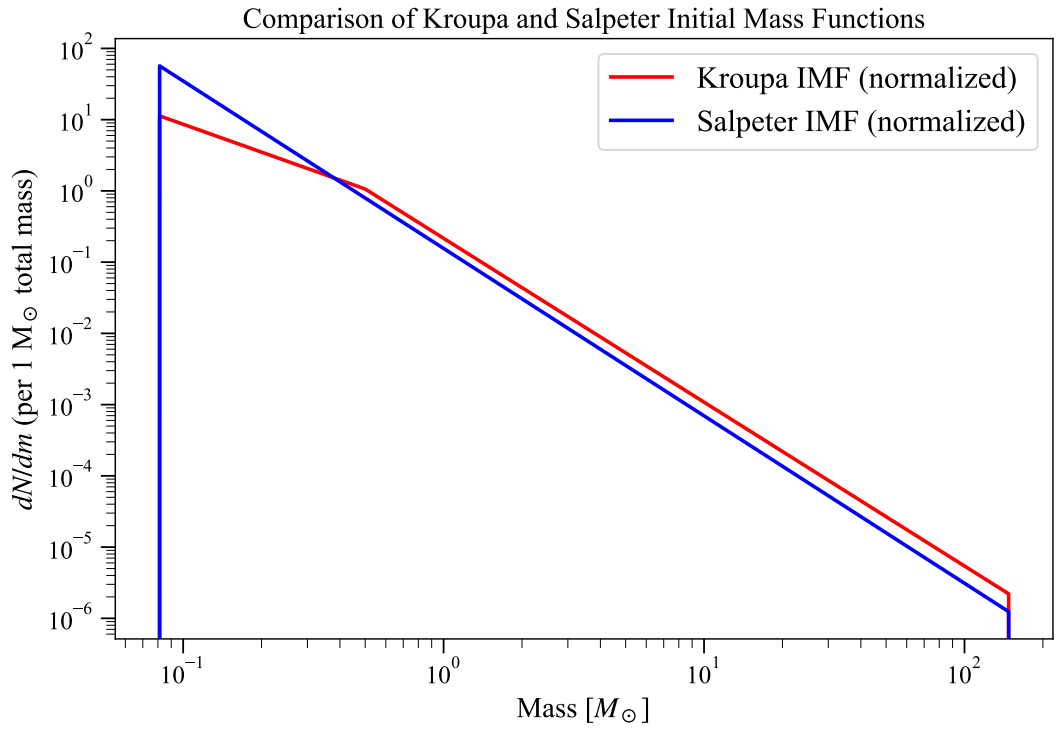

Fig. 1.1: IMF comparison according to Salpeter and Kroupa

1.1.1 Variation of IMF

The variability of the Initial Mass Function is a question that arose due to the dispersion of measured values of the power index α. If the IMF were universal, the distribution of values would be expected to follow a Gaussian curve, with the mean value corresponding to the actual IMF. In such a case, the dispersion would be caused only by measurement uncertainties. However, the actual observations did not meet these expectations, showing a much wider dispersion. This raises the question of whether this reflects real physical variations of the IMF or systematic measurement errors [6].

A more detailed discussion concerning the measurement of the initial mass function (IMF) and the primary systematic uncertainties is provided in [4] and the review [5], along with forthcoming encyclopedia entries [11].

Various IMF variations have been studied across diverse environments using a range of methods. These functions have been parametrized based on distinct stellar populations, star clusters, or integrated-light techniques, combining stellar population modeling with dynamical or gravitational lensing constraints. The interpretation of these results is often affected by systematic uncertainties and degeneracies [4, 5, 6].

For the Milky Way, recent studies based on star counts in the vicinity of the Sun suggest that the IMF may depend on the metallicity and age of the stars [13].

The dispersion of the resulting data could have been caused by several indirect factors. The first factor involves massive stars that migrate to the center of the cluster, where they can be ejected from the system during gravitational interactions, potentially distorting the observed mass distribution. High α values are most often measured in areas where it is more difficult to determine the age of stars or where it is necessary to use luminosity-to-mass conversion. Variability is also theoretically controversial due to metallicity and the physical conditions in molecular clouds. Under low-metallicity conditions, gas cooling is less efficient. For this reason, it leads to a higher Jeans mass and can thus shift the characteristic mass of objects to higher

values. This claim is associated with the first generation of stars (Population III). However, observations still do not find a systematic connection with changes in the IMF slope in the massive-star regime [14]. In light of these persistent uncertainties in the massive-star regime, this thesis adopts a set of IMF variations to bracket the potential range of the carbon-burning RSG population in the Milky Way, accounting for the possible systematic deviations from a universal model.

The idea of variability generally arises from empirical data and a theoretical understanding of the physical conditions in a given environment. Nevertheless, for massive stars, the IMF is generally viewed as invariant across various Milky Way settings, though findings suggesting potential variations—particularly in extreme environments—remain a topic of intense discussion [6].

In the context of IMF variability, the terms 'top-heavy' and 'top-light' are essential, as each indicates a different slope α and a different proportion of massive stars. If $\alpha = 1.6 \pm 0.1$, there is a predominance of massive stars, referred to as top-heavy. Conversely, if the number of massive stars is lower than the standard representation, it is termed top-light, with $\alpha = 2.7 \pm 0.1$ These values are used here as illustrative bracketing cases rather than global representations. [6][11]

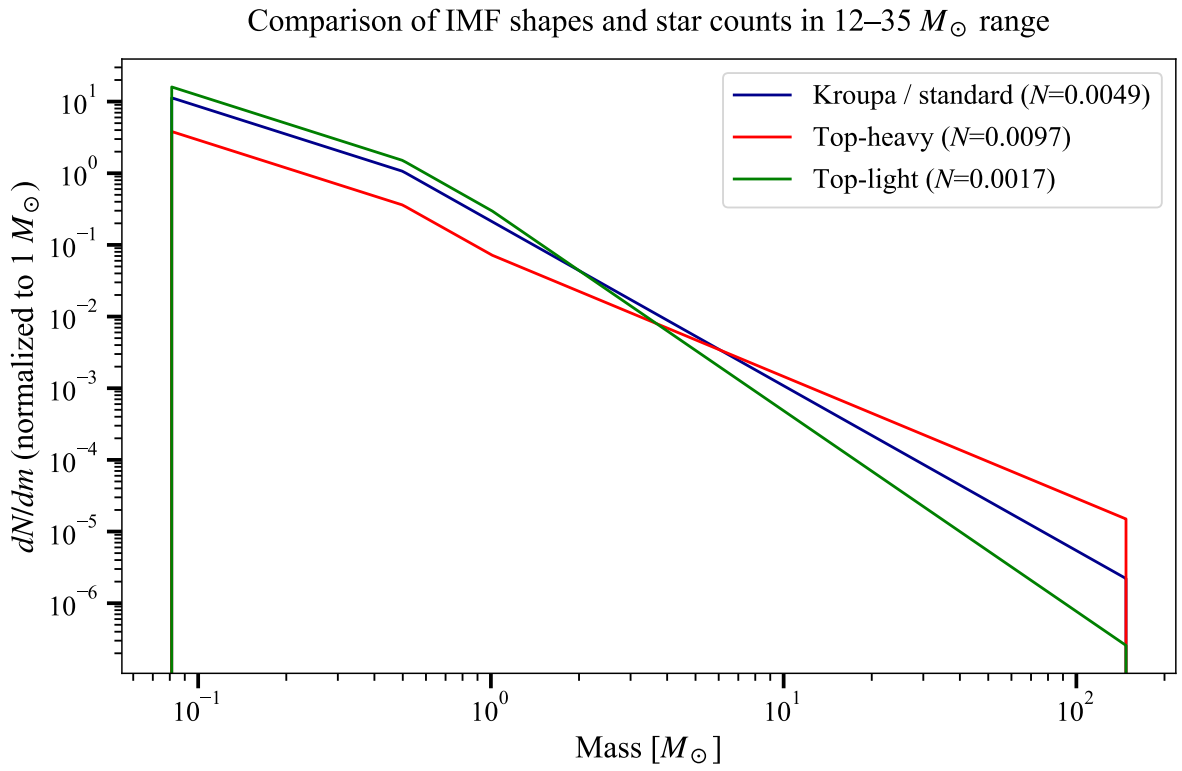

Fig. 1.2: IMF comparison according to Kroupa standard, top-heavy and top-light

Figure 1.2 shows a comparison of the Kroupa IMF with different variants. A change in the power-law index leads to a different slope and thus a different number of stars at a given mass. A top-heavy IMF, with a lower index and a flatter slope, results in a larger relative number of massive stars, while a top-light IMF, with a higher index and a steeper slope, results in fewer massive stars.

1.2 Red supergiants

Red supergiants (RSGs) are stars with initial masses ranging from approximately 8 to 25(–30) $M_{\odot}$ that have already passed through the main-sequence phase. This mass range is inherently model-dependent, as the upper limit is significantly influenced by factors such as metallicity, rotation, and mass-loss rates. Consequently, stars with initial masses above 25–30 $M_{\odot}$ may not evolve into classical red supergiants. However, various theoretical models and studies of high-mass stars suggest that this limit is not strictly fixed and can be higher under certain conditions. In this work, an upper limit of 35 $M_{\odot}$ was adopted to ensure broader coverage of potential RSG progenitors and to account for overall uncertainties in stellar evolution. RSGs are located in the upper right region of the Hertzsprung–Russell diagram. Stars in this position exhibit high luminosity, ranging between 10^4 and 10^5 $L_{\odot}$, and a low effective temperature of approximately 3500–4000 K. [15] Stars ranging from late O-type to early B-type become RSGs after exhausting the central hydrogen in their cores during the main sequence (MS) phase. [16]

The evolution toward the RSG stage in massive stars is strongly influenced by their membership in binary systems. Interactions with a companion, specifically through Roche lobe overflow, can cause a star to lose its hydrogen envelope before it ever reaches the dimensions of a red supergiant. In such cases, the star completely bypasses the RSG phase and evolves directly into a stripped helium core. Consequently, the frequency of RSGs within galactic populations is directly dependent on the distribution of orbital separations in binary systems. [17]

RSGs are characterized by a large expansion of the stellar envelope, which can reach up to a thousands solar radii ($R_{\odot}$). After the star exhausts all the hydrogen in its core, the core contracts. This contraction releases energy that expands the star's envelope. This behavior is referred to as the mirror effect [18].

While the envelope cools, the opposite occurs in the central regions, where heating takes place during helium burning. The envelope thus becomes highly convective, as the energy produced in the core cannot be effectively transported through the expanded envelope by radiation alone [16].

RSG atmospheres are very dynamic, inhomogeneous, and spatially extensive due to low surface gravity and extensive convection. A key feature of RSGs is intense convection, which manifests on the surface of stars as convective cells or granulation. This intense convection, combined with internal pulsations, disrupts hydrostatic equilibrium and leads to significant stellar variability.

Due to the complex dynamics of the stellar atmospheres of red supergiants, it is very difficult to determine their parameters. . [19, 20] One of the factors influencing the observed properties of RSGs, aside from their intrinsic structure, is the metallicity of the galaxy in which the star is located. The spectral type of an RSG shifts toward warmer types if the metallicity of the environment is lower. This phenomenon has been recorded, for example, in the Small Magellanic Cloud; in such environments, stars shift toward warmer spectral types and exhibit reduced mass-loss rates. These variations directly affect the star's classification and positioning on the Hertzsprung–Russell diagram [19].

The presence of dust in these layers increases the opacity of the environment, which further allows radiation pressure to transfer momentum to matter. By this process, the mass loss in RSGs is significantly influenced by means of stellar dust [20].

Material that leaves the star's atmosphere via stellar wind often does not disperse into the interstellar medium, but for a certain period of time, it forms a dense circumstellar environment around the star composed of gas and dust [19].

RSG-type stars are subject to a fundamental stability limit known as the Humphreys-Davidson limit. This limit indicates a boundary on the H-R diagram and thus defines the maximum luminosity at which stars can remain in the RSG phase. By exceeding this boundary, they would become unstable. Stars approaching this boundary are subjected to high radiation pressure, and the star is unable to retain its outer envelopes. The loss of these envelopes leads

to episodic mass loss. Thanks to this limit, it is possible to determine the maximum initial mass of stars that are capable of reaching the RSG phase [19].

Red supergiants are characterized by strong stellar winds, through which the star loses a significant amount of mass. Mass-loss rates can reach 10^{-6} to $10^{-4}\,M_{\odot}\ \mathrm{yr}^{-1}$. Even small variations in mass can affect the final core mass. This mass loss affects the star's radius, reduces the hydrogen content in the envelope, and alters the density and temperature of the core. Consequently, mass loss influences the overall evolution and the final fate of the star, including the type of core collapse [16, 15].

RSGs go through several evolutionary phases. The first and longest phase is helium burning, which lasts several million years and is followed by core contraction. The second phase is carbon burning, which lasts hundreds to thousands of years. During this phase, neutrino emission becomes the dominant mechanism of energy loss (surpassing photon emission), significantly affecting the star's thermodynamic equilibrium in the advanced burning stages (C, Ne, O, Si). The penultimate stage is oxygen burning, which lasts only a few months, and the final, shortest phase is silicon burning. Although neutrino luminosity is highest during these last two stages, the probability of encountering such stars in the current snapshot population is negligible due to the extremely short duration of these burning phases. [15, 16]

Red supergiants are frequently identified as the progenitors of Type II-P supernovae. This specific explosion type is characterized by the presence of a massive, extended hydrogen envelope that RSGs retain until the end of their lives. When thermonuclear fusion in the core ceases, gravitational collapse occurs, generating a shock wave that ejects the star's outer layers into the surrounding medium. In Type II-P supernovae, this hydrogen is ionized during the explosion, making it opaque to radiation. As the expanding ejecta cools, a process known as recombination occurs, where electrons return to the atomic nuclei, rendering the hydrogen transparent once again. This recombination wave propagates from the outer edges of the material inward toward the center [16, 19].

1.2.1 Carbon-burning red supergiants

The carbon-burning phase in RSGs is an advanced phase of nuclear burning that begins after the helium in the core is exhausted. This phase can last hundreds to thousands of years. Compared to the previous phases, it is much shorter, but compared to the later phases, it is already a notable event. [21] The transient nature of this phase compared to the overall stellar lifetime is reflected in the HR diagram 3.2.

For carbon burning, compared to helium burning, a higher temperature and density of the core are required, as higher density increases the probability of collisions. After the helium is exhausted, the core therefore contracts, typical densities increase up to approximately 10^5 – 10^6 $\mathrm{g/cm^3}$, and the temperature increases up to around 5×10^8 K. The conditions in the stellar core depend on the star's initial mass, and the values provided serve only as a representative estimate for the RSG range [21, 22].

After helium exhaustion, the core consists mainly of ^{12}C and ^{16}O. The main nuclear reactions are $^{12}\mathrm{C} + {}^{12}\mathrm{C}$. The reaction of two carbon nuclei can result in several possible reaction channels. Neon (^{20}Ne) can be produced with an alpha particle (α) as a by-product. Sodium (^{23}Na) can be produced with a proton (p), and magnesium (^{24}Mg) with gamma radiation (γ). The resulting elements, such as neon, sodium, and magnesium, can then become fuel for subsequent burning phases [22].

As carbon burning takes place in the core, the shells from previous burning phases are located above it. Typically, these consist of a helium-burning shell and a hydrogen-burning shell. Therefore, RSGs exhibit a characteristic layer distribution known as an onion-like structure. Each layer has a different chemical composition; generally, the closer a layer is to the center, the higher its temperature and density. The shells can gradually expand away from the core, with their positions depending on the initial mass of the star.

The structure of a star above the carbon-burning core can be divided into several stages. First is the carbon-burning shell, where carbon burning occurs and the layer is usually convective. This is followed by a helium-burning shell, where the main process is the triple-alpha reaction. The main products of this layer are carbon and oxygen. The next layer is typically the hydrogen-burning shell, where hydrogen burning occurs primarily via the CNO cycle, producing helium. Finally, there is the outer envelope, which is a very extensive area of the star. Compared to the inner regions, it has a relatively low temperature and experiences significant mass loss due to stellar winds. The material in this layer is characterized by strong convection.

Another very important process in the core is neutrino emission. This can occur in several ways:

- pair annihilation—in this process, an electron and a positron ($e^- + e^+$) create a pair of neutrinos ($\nu + \bar{\nu}$)
- photoneutrino process—a photon (γ), when interacting with an electron (e^-), produces a pair of neutrinos ($\nu + \bar{\nu}$)
- plasma neutrinos—in which collective oscillations of electron plasma produce neutrinos.

For the carbon-burning stage of the RSGs studied in this work, pair annihilation is the dominant neutrino emission process [23].

One of the most important events of this phase is neutrino cooling. Neutrinos interact minimally with the stellar matter and immediately leave the star. One of the most important consequences is the energy loss caused by emitted neutrinos. This has a major impact on the entire star. As the core loses energy through the emission of neutrinos, the pressure drops, the core contracts, and the temperature increases[23, 22, 24].

The carbon-burning phase marks a significant moment. At this stage, the star becomes independent of its envelope. Because the core evolves in such a short time due to neutrino losses, the outer layers don't have enough time to react to the changes happening in the star's center. This decoupling – the separation of the core from the envelope – is the reason why the star's position on the HR diagram remains relatively unchanged during the carbon-burning phase[25]. This can be seen in Figure 3.2.

The energy balance in the carbon-burning phase depends on the ratio of energy produced by nuclear reactions to energy lost through neutrino emission. If the energy from nuclear reactions is higher than that from neutrino losses, it results in a stable core and carbon burning is convective. If, on the other hand, neutrino emission is greater, burning is radiative and no convection occurs [7].

1.3 Neutrino detectors

Detecting MeV and sub-MeV neutrinos emitted from astrophysical sources is extremely difficult due to the very weak interaction of neutrinos with matter. This requires a large detector mass with a target material that increases the probability of neutrino interactions, making background control essential. In neutrino measurements, we can distinguish between two types of background (signals that do not originate from the observed source).

We divide the background into two types:

- **Solar neutrinos** — an irreducible background consisting of neutrinos originating from the Sun, which pass through the Earth in enormous quantities. This type of background is impossible to eliminate because their energies are very similar to those emitted by the studied object, and they interact in a similar way.
- **Radiogenic backgrounds** – This is a type of background originating from the detector material itself or the surrounding environment. It mainly consists of gamma rays and beta particles emitted by radioactive isotopes, which can interfere with the neutrino signal.

This implies that the practical detectability of low-energy stellar neutrinos is strongly dependent on the detector threshold, radiopurity and analysis cuts.

When detecting astrophysical neutrinos, two types of detectors are most commonly used:

- **Water Cherenkov detectors** – Thanks to Cherenkov detectors, we are able to determine the direction of neutrinos, which emit Cherenkov radiation when interacting with water. Unfortunately, this type of detector has a relatively high energy threshold.
  - For better background reduction, water Cherenkov detectors are doped with gadolinium. Gadolinium has the ability to capture neutrons produced during inverse beta decay, which would otherwise attach to hydrogen. This proposal was first detailed in the paper by Beacom and Vagins (2004). [10]
  - Example: Hyper-Kamiokande [8]
    According to the technical report for the Hyper-Kamiokande project, the Cherenkov detector is described with a total target mass on the order of several $\times 10^2$ kilotons.
- **Liquid scintillator detectors** – Liquid scintillator detectors enable the measurement of even low-energy neutrinos. However, it is necessary to strongly suppress radioactive background, and these detectors generally lack directionality.
  - Example: Jiangmen Underground Neutrino Observatory (JUNO) [9]
    It is a 20-kiloton liquid scintillator detector. Its energy resolution is approximately $3\%/\sqrt{E(\mathrm{MeV})}$. This enables precise measurements in the MeV region but provides very limited directional information.

1.3.1 Detection of neutrinos from RSG

Neutrino production in red supergiants is most pronounced during the final phase of silicon burning, when energy losses are greatest. Although neutrino luminosity peaks during the silicon and oxygen burning phases, these periods are extremely short-lived, making the snapshot population of stars in these states negligible. In contrast, while the carbon-burning phase exhibits lower neutrino production, the likelihood of detection is significantly enhanced because this phase lasts hundreds to thousands of years. This increases the probability of such an object existing in the Galaxy at any given moment, thereby improving the overall prospects for neutrino detection. (Compared to previous longer periods, such as helium and hydrogen burning, neutrino production has increased significantly.)[15]

Neutrinos in the C-burning phase of RSGs have very low energies, less than 1 MeV. Their detection is therefore very sensitive to background and low energy thresholds. Detectability studies in the work of G. Seong (2025) [7] suggest the development of observations for this type of neutrino. Very large detectors with low thresholds could achieve on the order of tens of events per year in the future for sufficiently close sources. One of the significant factors in their success is the background problem, as the signal is weaker in comparison.

Detecting such a signal using current detectors is extremely difficult for many reasons. Water Cherenkov detectors have a much higher detection threshold, and scintillation detectors are unable to obtain information regarding neutrino direction because their light emission is isotropic. Hybrid detectors, which combine water Cherenkov and scintillation technologies, overcome some of these problems; however, they are still not perfect. Hybrid detectors can detect neutrinos with a low energy threshold while simultaneously determining their direction using Cherenkov radiation. These detectors typically operate using water-based liquid scintillators (WbLS)[26] and fast Large Area Picosecond Photodetectors (LAPPDs) [27].

Hybrid detectors

Current neutrino detectors still face several fundamental limitations for certain types of neutrino experiments. Hybrid detectors, currently in the development and prototyping stages, serve as a concept designed to overcome the individual limitations of both water Cherenkov and liquid scintillation detectors.

Hybrid detectors are a combination of water Cherenkov and scintillation detectors. Thanks to this combination, the detector can record neutrinos with a low energy signature while simultaneously determining their direction [15].

Detection is based on the emission of two distinct types of photons following an elastic neutrino-electron scattering event. The electron emits Cherenkov light and, simultaneously, fluorescent (scintillation) photons, each of which carries different information. Cherenkov photons are emitted in the direction of the electron's momentum, allowing for directional reconstruction, while scintillation photons are emitted isotropically in larger quantities, ensuring high detection efficiency [28, 29].

Hybrid detectors typically use water-based liquid scintillator (WbLS) as the detection medium. This is a mixture of water and liquid scintillator, where the water component facilitates the propagation of Cherenkov photons, while the scintillator provides the medium for scintillation photons [26].

These photons can be separated thanks to the time delay that occurs between them. Cherenkov photons are emitted promptly, while scintillation photons are emitted with a characteristic delay. LAPPDs are used to record this, as they are capable of resolving the delay between the emission of both types of photons. The time resolution of an LAPPD is 25 ps [27].

Although hybrid detectors offer significant theoretical advantages, they remain a developmental concept. In this work, their inclusion is primarily illustrative of the potential of future experiments; therefore, the calculations should be interpreted as idealized estimates assuming advanced technological conditions.

e

2 METHODOLOGY

2.1 Variants of the IMF and Their Impact on the Massive Star Population

The original idea of the IMF suggested that it is approximately invariant in many Milky Way environments; however, recent studies point to the possibility that it may vary in extreme environments depending on conditions such as gas density, temperature, or UV radiation intensity, though such evidence remains debated [4, 5, 11].

In this thesis, we do not adopt specific environment-dependent IMF prescriptions. Instead, we account for the potential impact of non-universality by varying the power-law index. Since our analysis focuses on stars in the mass range of 12–35 $M_\odot$, we specifically vary the slope index α_3, which describes the distribution for stars more massive than 0.5 $M_\odot$. In this work, we consider three specific values for the slope index: $\alpha_3 = 2.3$ for the standard Kroupa IMF, $\alpha_3 = 1.7$ for the top-heavy variant, and $\alpha_3 = 2.8$ for the top-light variant.

Different IMF shapes have been discussed for different environments and epochs (e.g. as a function of metallicity, gas density, temperature, turbulence, and feedback), but establishing a unique, spatially varying IMF model for the Milky Way remains challenging [4, 5]. Therefore, rather than adopting a specific Milky-Way-by-environment IMF prescription, we explore the possible impact of IMF non-universality on the massive-star population by comparing three illustrative high-mass IMF slopes: a standard (Kroupa-like) case, a top-heavy case, and a top-light case.

This calculation tests the sensitivity of our results to the high-mass slope, but it does not model a spatially varying IMF in the Milky Way.

2.2 Stellar Lifetimes and the Carbon-Burning Phase

Stellar lifetimes were extracted from PARSEC stellar evolution tracks and visualized using Hertzsprung–Russell (HR) diagrams. The data obtained from the PARSEC v2.0 database [30, 31] were reduced to stellar models with masses in the range of 12–35 $M_\odot$, metallicity $Z = 0.01$, rotation ROT = 0, and initial helium abundance $Y = 0.267$. The metallicity $Z = 0.01$ was chosen as it represents typical disk populations and falls within the range of sub-solar metallicities found in the Milky Way. If a higher Z value is defined, the stars shift toward the cooler part of the HR diagram and simultaneously exhibit a longer lifetime, although the character of the curve remains unchanged.

In addition to identifying the late evolutionary stages and the carbon-burning phase, key milestones along the main sequence were also recorded. The Zero Age Main Sequence (ZAMS) was defined as the starting point of the computational model. The Terminal Age Main Sequence (TAMS), marking the end of the main sequence, was determined as the moment when the central hydrogen mass fraction X_c fell below 10^{-4}. This depletion threshold represents the complete exhaustion of hydrogen in the core and the subsequent transition to the helium-burning phase.

In the processed code, the onset of the carbon-burning phase was determined using hierarchically defined points to ensure an unambiguous definition. First, we established core helium exhaustion, defined as the moment when the central mass fraction of helium Y_{cen} fell below 10^{-4}. This point defined the necessary stage after which the search for carbon burning was initiated.

The actual beginning of the carbon-burning phase was then operationally defined as the first decrease of the central carbon abundance $X_{C,cen}$ by more than 1% relative to its previously reached maximum. The sensitivity of the phase duration to the chosen threshold increases with the initial stellar mass. While the difference is minimal for lower-mass stars, it becomes significantly more pronounced for stars with higher initial masses. The chosen drop criterion

allows us to reliably identify the onset of burning within the model's discrete time steps. In cases where the central carbon abundance was unavailable, the condition $\log_{10} T_c \geq 8.65$ was used as an approximate proxy for the onset of this phase. This procedure allowed for a precise determination of the carbon burning phase duration based on the physical parameters of the stellar core.

For the calculations, it was necessary to use the AGE column to determine the stellar lifespan, LOG_TE and LOG_L for effective temperature and luminosity, The X_CEN column (representing central hydrogen abundance X_c) to determine the end of the main sequence, Y_CEN (representing central helium abundance Y_c) for the end of helium burning, XC_CEN (representing central carbon abundance $X_{C,cen}$) to monitor the carbon burning phase, and LOG_TC ($\log_{10} T_c$), which served as a backup proxy for the onset of carbon burning.

2.3 Estimation of the Snapshot Population of Carbon-Burning Stars

Based on the stellar lifetimes and phase boundaries determined in the previous section 2.2, the total number of stars of a given type in the MW can be estimated by combining the numerical fraction of the given IMF, the star formation rate, and the duration of the given phase. The number fraction for stars with masses between12–35 $M_\odot$ is calculated in section 2.1. The carbon burning duration for stars in the range 12–35 $M_\odot$ is given in section 2.2

In general, we can write the calculation for the number of stars in a given phase using equation (2.1).

$$N_{\text{now}} \approx \psi \int_{12}^{35} \xi(m) \cdot \Delta t_C(m)\, dm \tag{2.1}$$

where $\xi(m)$ denotes the stellar initial mass function [stars $M_\odot^{-1}$], ψ represents the total star formation rate (SFR) [$M_\odot$ yr^{-1}], and $\Delta t_C(m)$ is the duration of the C-burning phase for a star of mass m [yr]. This calculation assumes a continuous stellar mass distribution. In practice, however, stellar evolution models provide data only for discrete masses, so the integral is approximated by a summation over the mass bins. To maintain physical consistency, the IMF-based weighting and the phase duration must remain coupled within the sum, as both parameters vary significantly with stellar mass.

$$N_{\text{now}} \approx \text{SFR} \sum_i w_i \cdot \Delta t_{C,i}, \tag{2.2}$$

where w_i represents the number fraction of stars formed within the i-th mass bin. By multiplying the total SFR and the weight w_i, we obtain the star formation rate in the given mass interval. The IMF is normalized to a total formed stellar mass of 1 $M_\odot$. This weight w_i is derived from the integral of the normalized IMF ($\xi(m)$) over the mass interval of the i-th bin.

$$w_i = \int_{m_i^-}^{m_i^+} \xi(m)\, \mathrm{d}m. \tag{2.3}$$

$\Delta t_{C,i}$ denotes the duration of the carbon-burning phase for RSGs corresponding to the given mass interval, and SFR defines the current star formation rate in the MW. This formulation, representing a mass-bin-weighted sum, ensures that lower-mass stars, which are more numerous due to the IMF but have different burning timescales, are correctly weighted according to their relative contribution. To ensure dimensional consistency, the IMF function is normalized to $1\,M_\odot$, and multiplying it by the SFR parameter (in $1\,M_\odot$/year) converts the relative number of stars formed into their actual formation rate. Subsequent multiplication by the lifetime Δt yields the resulting number of stars in a given evolutionary phase within the current 'snapshot' of the Galaxy.

We can consider the SFR to be constant in this calculation, as stars in the mass range of 12–35 $M_\odot$ are short-lived and any past variations in the SFR are negligible. The expected snapshot number of red supergiants in the carbon-burning phase is estimated by summing over discrete mass bins. For each interval, the star formation rate in that range is multiplied by the duration of the carbon-burning phase corresponding to the specific stellar mass. The change in the SFR value is directly proportional to N_{now}. This direct proportionality implies that any uncertainty in the star formation rate estimate is linearly transferred to the resulting star counts.

If we consider the star formation rate in the Milky Way (SFR_{MW}), the calculation may be based on the value $SFR_{MW} = 1.9 \pm 0.4\ M_\odot\,yr^{-1}$. [32]. Since the present number of stars (N_{now}) corresponds directly to this rate, the 20% uncertainty in SFR is propagated linearly into the "expected number of stars within a given time frame. For the purposes of the calculation, SFR_{MW} can be considered constant over a horizon of the last 20 million years. This assertion is based on the fact that the lifetimes of the stars under consideration do not exceed 20 Myr, and their present existence corresponds exclusively to this steady value.

2.4 Monte-Carlo simulation

The Monte Carlo simulation presented in this section, which models the distribution of red supergiants in the Milky Way, is structured into three key steps. The first part aims to establish the total Galactic population by estimating the expected number of RSGs in the carbon-burning phase, based on the star formation rate and the initial mass function. The second part of this chapter focuses on their spatial distribution using a multi-component geometric model of the Galaxy. In the final step, by generating Galactic snapshots, we determine the local abundance of sources and use these data to calculate the statistical probability of the occurrence of an RSG in the carbon-burning phase within a 1 kpc radius of the Sun.

The detection of the neutrino flux emitted by red supergiants is very difficult due to their low energy. To simplify the calculation, it is possible to use only the statistical abundance of stars located within a distance of one kiloparsec from Earth. Determining the exact phase of a star is imprecise and uncertain, so we cannot determine the exact population of red supergiants in the carbon-burning phase at a given distance. For this calculation, the most accurate method is to use a Monte Carlo simulation to estimate the expected occurrence of RSGs in the carbon-burning phase within a certain area. This simulation builds upon the total galactic population counts derived in Sect. 2.3 and distributes them spatially to evaluate local abundances. The entire simulation was developed using the Python programming language, utilizing libraries such as dataclasses, pathlib, and annotations as part of a custom-written framework for all performed calculations.

2.4.1 Simulation Framework and Statistical Approach

Monte Carlo simulation is a mathematical and statistical method widely used in physics and astrophysics to address complex and often unsolvable mathematical problems. It works on the principle of evaluating as many scenarios as possible according to predefined probability distributions, followed by a statistical evaluation. The result is not a single number, but a distribution of possible values. From this distribution, it is possible to determine the average value, statistical deviation, or confidence interval.

As a key part of this thesis, a custom Python-based code was developed to function as a discrete simulator, generating instantaneous snapshots of the Galaxy by integrating selected Initial Mass Functions (IMF) and spatial density profiles. Instead of fixed counts, the number of stars for each mass distribution is generated using a Poisson distribution. This allows for a more natural simulation with statistical fluctuations across individual snapshots. To ensure

statistical reliability and eliminate random fluctuations, the algorithm generates 50 000 independent snapshots for each IMF type. The number of 50,000 trials was chosen as the point where the simulation results achieved convergence; further increasing the number of iterations did not significantly alter the outcomes. This approach allows us to transition from the global theoretical average population, as defined in Eq. 2.1, to a representation of the Galaxy based on the random spatial distribution of stars within it. The probabilistic representation of the red supergiant (RSG) population during the carbon-burning phase in the Milky Way is derived using these Monte Carlo simulations. Data processing using this approach provides a representative distribution of the stellar population and a statistically significant estimate for the expected occupancy of target objects.

Given that the expected number of stars in the carbon-burning phase within a 1 kpc radius is very low, the resulting distribution exhibits the characteristic features of a Poisson process. Based on this assumption, the Monte Carlo framework allows us to account for the discrete nature of stellar occurrences. Within a given snapshot, the presence of these stars is naturally described by a discrete counting distribution where the number of sources N is always a non-negative integer.

Since the expected number of RSGs in the carbon-burning phase within a 1 kpc radius is smaller than unity, the results must be interpreted probabilistically. In this regime, the expected mean number of sources, λ, is a key quantity. According to the Poisson distribution $N \sim \text{Poisson}(\lambda)$, it is possible to define the probability of finding a specific number of stars in the local volume. The probability of finding no stars within a 1 kpc radius at a given time is defined by Eq. 2.4, and the probability of finding at least one star within the same radius is defined by Eq. 2.5.

$$P(N = 0) = e^{-\lambda}, \tag{2.4}$$

$$P(N \geq 1) = 1 - e^{-\lambda}. \tag{2.5}$$

By employing this probabilistic approach, we avoid the inconsistencies of Gaussian statistics, which are unsuitable for rare events and would incorrectly imply the possibility of negative star counts. Thanks to the Poissonian framework, the simulation remains physically consistent with the discrete nature of the stellar population.

2.4.2 Stellar Population and Spatial Modeling

As defined in the code, the simulation operates in a state of dynamic equilibrium (steady-state). Based on a constant star formation rate of $\text{SFR} = 1.9\,\text{M}_\odot\,\text{yr}^{-1}$, the model generates a population of stars that have formed within the last 20 million years. This time frame was chosen because the maximum lifetime of the stars under consideration does not exceed this period. This approach ensures a galactic snapshot that faithfully represents the instantaneous state, where stars are captured in various evolutionary stages depending on their randomly assigned age and mass.

The Initial Mass Function (IMF) serves as the primary parameter for the Monte Carlo integration. For each simulation, the code samples the mass distribution to determine the contribution of different stellar mass intervals to the total population. This mass is decisive for determining the star's evolutionary track and, specifically, the duration of its carbon-burning phase (Δt_C) as defined by the PARSEC database.To ensure computational efficiency and physical robustness, the simulation does not assign individual ages to every star in the Galaxy. Instead, it utilizes a probabilistic approach based on the assumption of a steady-state Star Formation Rate (SFR). The likelihood of a star being in the carbon-burning phase is defined by the ratio of that phase's duration to the total stellar lifetime. By integrating this probability across the sampled mass spectrum and the spatial model of the Milky Way, the code calculates a statistical expectation value λ for the local neighborhood. This λ represents the mean number

of stars expected in the given volume and serves as the basis for the Poissonian interpretation, allowing us to quantify the probability of detecting zero, one, or multiple sources at any given snapshot in time.

In this work, the Monte Carlo method was employed to repeatedly generate stellar populations in the Milky Way according to a defined density profile $\rho(r)$. The developed algorithm utilizes a random sampling based on the inverse transform sampling method to assign spatial coordinates to each object. Based on this stochastic distribution, the statistical frequency of stars within a defined kiloparsec interval was subsequently determined. This approach allowed for a realistic representation of the spatial distribution, defined the dispersion of objects, and enabled a statistical evaluation of the expected occurrence of rare evolutionary phases within the solar neighborhood.

The resulting spatial distribution and the derived expected number of sources, λ, serve as key inputs for calculating neutrino fluxes and their detection rates in Sect. 2.5.

2.4.3 Geometric Model of the Milky Way

To calculate the number of RSGs in the C-burning phase, it is necessary to define the distribution of stars and mass within the Milky Way (MW). For the purposes of the Monte Carlo (MC) simulation, the MW is modeled using a static geometric disk, without dynamical evolution. This approach treats the stellar distribution as a probability density field rather than a dynamical mass model, focusing on an instantaneous snapshot of the population while neglecting stellar dynamics.

One of the cornerstones of the Monte Carlo model for calculating the RSG population is the definition of the stellar density distribution, whereas the exact position of each star remains stochastic. The radial stellar density in the galactic plane is given by Equation 2.6 and decreases exponentially with galactocentric distance. This relationship ensures that the stellar distribution is non-uniform, with the concentration decreasing towards the galactic periphery. In the model, a value of $h_R = 1.8$ kpc was used. This value was chosen to reflect the stronger concentration of young stars, such as RSGs, toward the center of the Milky Way.

$$\rho(r) = \rho_0 \exp\left(-\frac{r}{h_R}\right) \tag{2.6}$$

The probability of finding a star decreases exponentially with its distance from the galactic center, as illustrated in Figure 2.1. For RSGs, this decline is particularly pronounced; as relatively young stars, they are more densely concentrated toward the inner regions of the galaxy.

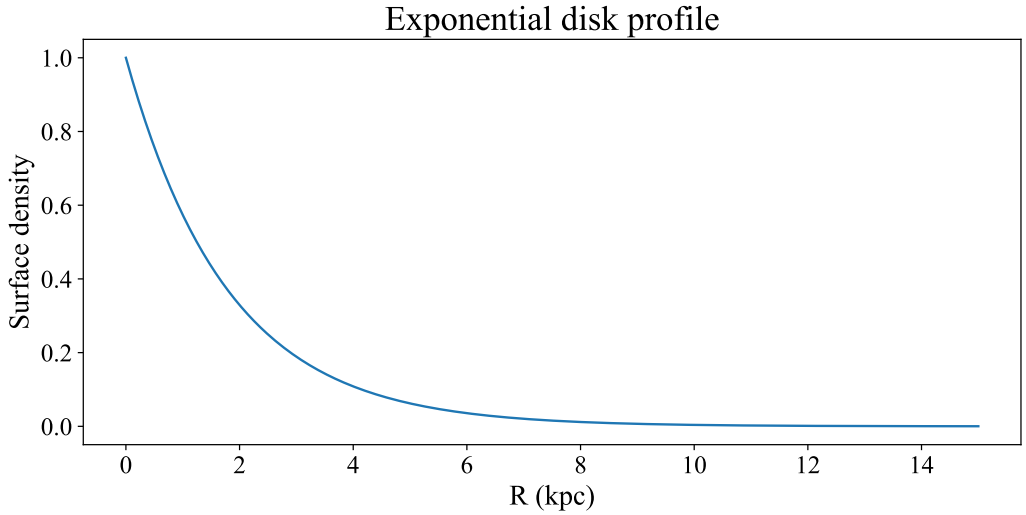

Fig. 2.1: Theoretical profile of the surface density of the stellar population in the galactic disk

The stellar distribution further depends on the parameterization of four spiral arms, as described by Equation 2.7 [33, 34]. The pitch angle ψ is set to 12°, which defines the radial growth and angular position of the arms [35, 36]. The stars are distributed relative to these arms using a Gaussian profile with a standard deviation of 0.3 kpc. [37, 38] This region contains a significant portion of the Milky Way's population of young stars.

$$R(\phi) = R_{ref} \exp((\phi - \phi_0) \tan(\psi)) \tag{2.7}$$

The distribution of the spiral arms in the MW within the galactic plane (x, y), as shown in Figure 2.2, determines the loci around which stars are modeled using a Gaussian profile. The arms are constrained by radial boundaries of 3 and 13 kpc, which correspond to the observed extent of the spiral structure in the Milky Way.

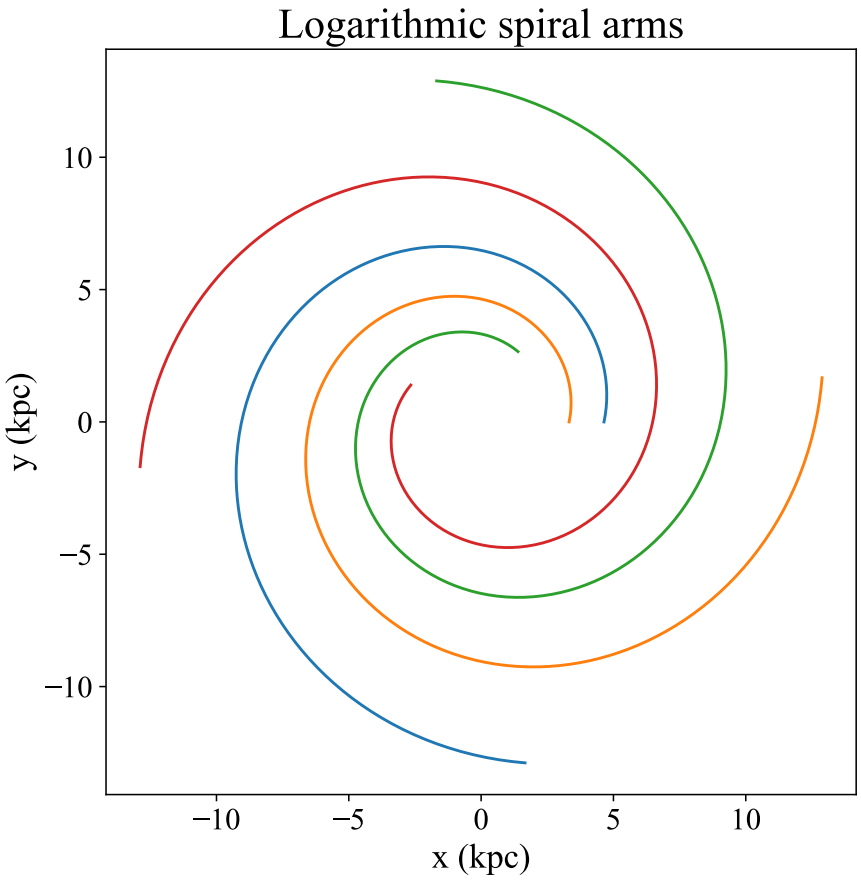

Fig. 2.2: Geometric structure of four logarithmic spiral arms in the galactic plane (x, y) for a pitch angle of $\psi = 12°$.

Additional stars are located within the molecular ring. This structure is modeled using a Gaussian distribution centered at 4.5 kpc with a width (standard deviation) of 0.5 kpc. While this region is a major site of star formation, it represents a secondary contribution to the total RSG population compared to the more prominent spiral arms.

The overall spatial structure is defined by the exponential disk, the spiral arms, and the molecular ring, collectively illustrated in Figure 2.3. This schematic diagram represents the geometric framework of the MW used for populating stars in the Monte Carlo simulation and defines the Sun's position relative to these regions. It is important to note that the adopted values—such as the number of arms, pitch angle, arm width, and radial range—should be regarded as physically motivated values within a simplified toy model. These do not represent a new fit to the detailed spiral structure of the Milky Way.

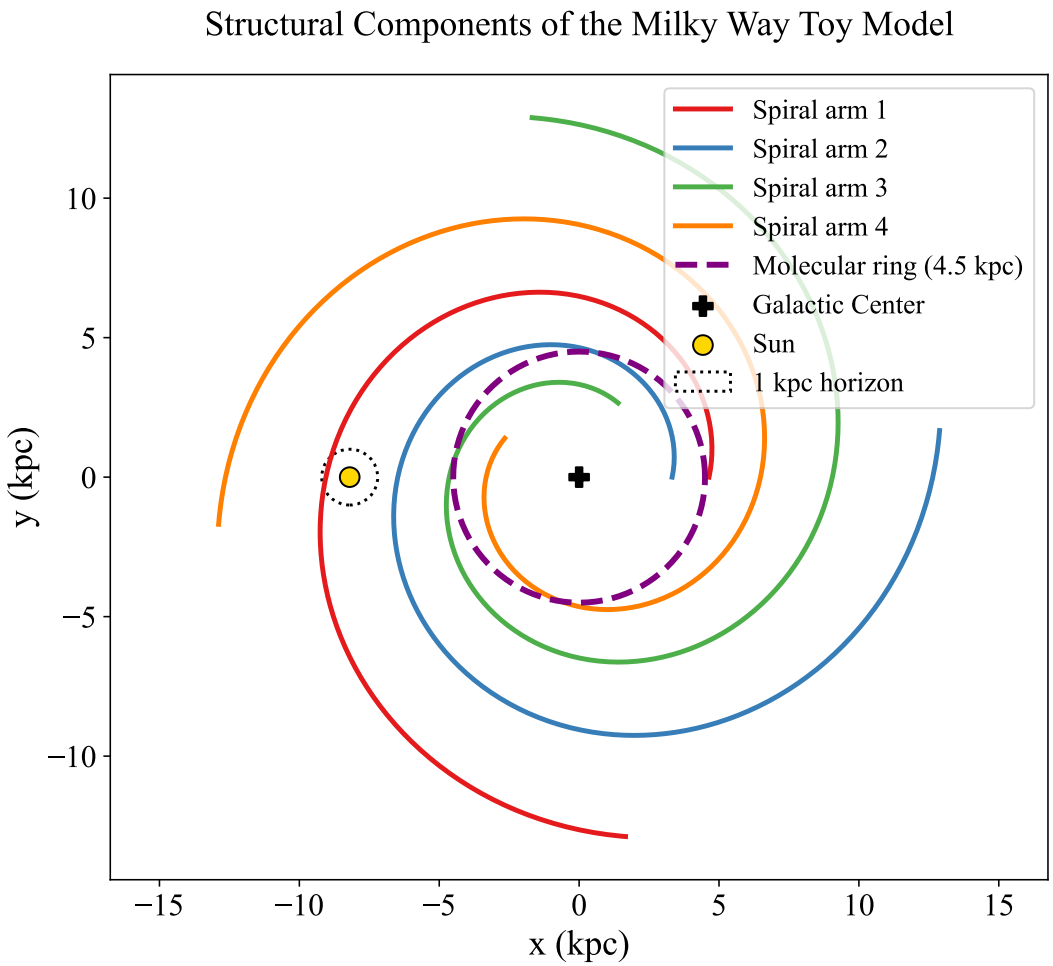

Fig. 2.3: Visualization of the spiral arms, the molecular ring, and the position of the Sun in a model of the Milky Way.

A comprehensive model of the stellar mass distribution along the galactic structure generates a continuous field that accounts for the statistical probability of stellar occurrence at any given location in the galactic plane. Figure 2.4 demonstrates the concentration of stars within the spiral arms and the molecular ring.

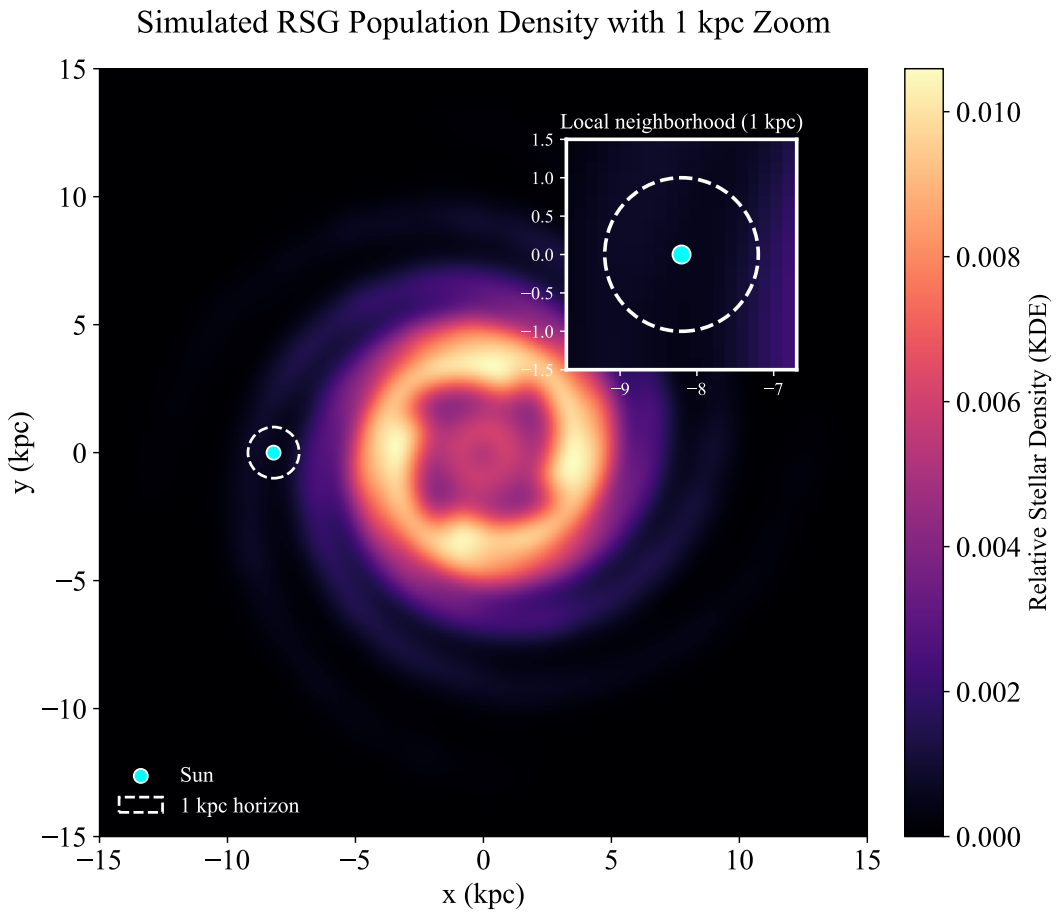

Fig. 2.4: Spatial distribution of a simulated red supergiant population in the galactic plane.

In the calculation, the MW is approximated as a 2D model defined by Cartesian coordinates (x, y). To determine the expected presence of stars within a 1 kpc radius of the observer, the Sun's position is set at the standard coordinates $(x, y) = (-8.2, 0.0)$ kpc. The sampled region is defined as a galactic cylinder that extends through the entire thickness of the disk rather than a sphere. Consequently, this volume includes all stars within the specified distance from the Sun as projected onto the galactic plane. The low stellar density near the Sun shown on the map and in the detailed inset visually matches the calculated values from the simulation in Table 3.5

2.5 Neutrino flux from RSG and detection of thermal neutrinos

Red Supergiants (RSGs) in the carbon-burning phase produce a significant amount of neutrinos. Although the neutrino flux is lower than in later evolutionary stages, this period is particularly suitable for detection due to its duration, which can last between 100 and 1000 years. Consequently, the probability of a star being in this specific burning phase is higher, making the potential detection of neutrinos more likely. Thermal processes are dominant during this stage. For the calculation of the neutrino flux of this type, a population of stars within a 1 kpc radius is considered, following [15]. The specific distributions of stars employed in this study are generated via the custom Monte Carlo simulation detailed in Section 2.4.

Within our model, we assume elastic neutrino-electron scattering as the primary detection channel. For the calculation of converting neutrino flux into detectable events, we use a simplified

estimate that does not account for background noise. A comprehensive evaluation of the detector response will be replaced in the future by a precise model based on [7], which will incorporate the specific behavior of the detector.

2.5.1 A theoretical model of neutrino flux

Calculating the neutrino flux required several approximations; the procedure employed here replicates [15] only marginally, utilizing numerous simplifications. The calculations are based on the assumption that the neutrino energy distribution follows the Fermi-Dirac statistics, which serves as a robust approximation for neutrinos generated via thermal processes, specifically electron-positron pair annihilation, which dominates the neutrino luminosity during the carbon-burning phase in Red Supergiants (RSGs).

In the code, the spectrum is defined by the relation 2.8, where T_ν represents the effective neutrino temperature. The model utilizes an effective neutrino temperature of $T_\nu = 0.1905$ MeV. This value is selected based on the Fermi-Dirac energy spectrum to approximate the peak at 0.6 MeV, as reported in [15]

$$f(E) = \frac{E^2}{\exp(E/T_\nu) + 1} \tag{2.8}$$

Since this relation determines only the relative energy distribution, a normalization factor is introduced, which is obtained by integrating the function $f(E)$ approximated over the finite energy range (0, 15 MeV). This integration limit was chosen to cover the dominant portion of the energy spectrum produced during the C-burning phase.

An important parameter of neutrinos is the average energy E_{avg}, which serves as a key factor in the model for calculating the interaction cross-section. It can be calculated numerically from the resulting spectrum as a derived quantity using equation 2.11.

The calculation assumes a water-based liquid scintillator (WbLS) detector with a total mass of M_{det}. The electron antineutrino flux ($\bar{\nu}_e$) for a star at a distance d (in kpc) is then defined by relation 2.9. The calculation is performed based on a reference flux $\Phi_{200pc} = 10^5$ cm^{-2}s^{-1} for a star like Betelgeuse (at 0.2 kpc). The reference flux Φ_{200pc} is an adopted value from [15], serving as a normalization constant for our model.

$$\Phi_{total}(d) = \Phi_{200pc} \cdot \left(\frac{0.2}{d}\right)^2 \tag{2.9}$$

To account for the dependence of the flux on the source distance, we utilized the Monte Carlo simulation to integrate the individual contributions of the simulated stellar population. By leveraging the specific positions of stars within each snapshot, we calculated their individual fluxes, thereby incorporating the stochastic spatial distribution within the 1 kpc volume. To illustrate the impact of distance on the flux, our algorithm was used to simulate the flux scaling of a single star; the resulting data, presented in Table 2.1, demonstrate the relationship $\Phi(r) \propto 1/r^2$ in Figure 3.5.

Distance d [kpc]	**Flux Φ [cm^{-2}s^{-1}]**
1.00	4.00×10^3
0.75	7.11×10^3
0.50	1.60×10^4
0.34	3.46×10^4
0.20	1.00×10^5
0.10	4.00×10^5

Tab. 2.1: Illustrative values of neutrino flux scaling for a single star at various distances, demonstrating the non-linear relationship used to verify the model consistency.

The resulting differential flux $\frac{d\Phi}{dE}$ is established by relation 2.10. It defines the number of neutrinos per cm^2 per second per MeV.

$$\frac{d\Phi}{dE} = \Phi_{total}(d) \cdot \frac{f(E)}{\int_0^{15\,\mathrm{MeV}} f(E)\,dE} \tag{2.10}$$

The total expected flux from the RSG population (Φ_{tot}) is determined by aggregating the fluxes of all carbon-burning RSGs generated within the Monte Carlo simulation inside the 1 kpc radius. This approach ensures that the higher flux contributions from stars located closer to Earth are physically represented in the final results. The resulting neutrino flux values for different IMF types are presented in Table 3.7. While the flux of a single star and the average neutrino energy are determined by internal stellar physics, the total flux depends on the chosen Initial Mass Function (IMF), which predicts a different statistical abundance of stars currently in the given evolutionary phase.

The energy spectrum is approximated using a Fermi-Dirac distribution with a uniform effective temperature, rather than a realistic spectrum which may exhibit deviations from the ideal shape and vary depending on the neutrino flavor. Furthermore, the integration is performed over a finite energy interval that sufficiently covers the relevant part of the spectrum, instead of integrating over the entire energy range. Nevertheless, the described approach provides a consistent estimate of the neutrino flux from a Red Supergiant (RSG) during the carbon-burning phase.

The distribution of stars from the Monte Carlo simulation as a function of distance from the Sun for individual IMF types is shown in Figure 2.5. The histogram illustrates the increase in the number of stars with increasing distance from the Sun. The differences in the absolute number of stars found between various IMF types demonstrate the sensitivity of the models, which has a direct impact on the neutrino flux and its detection.

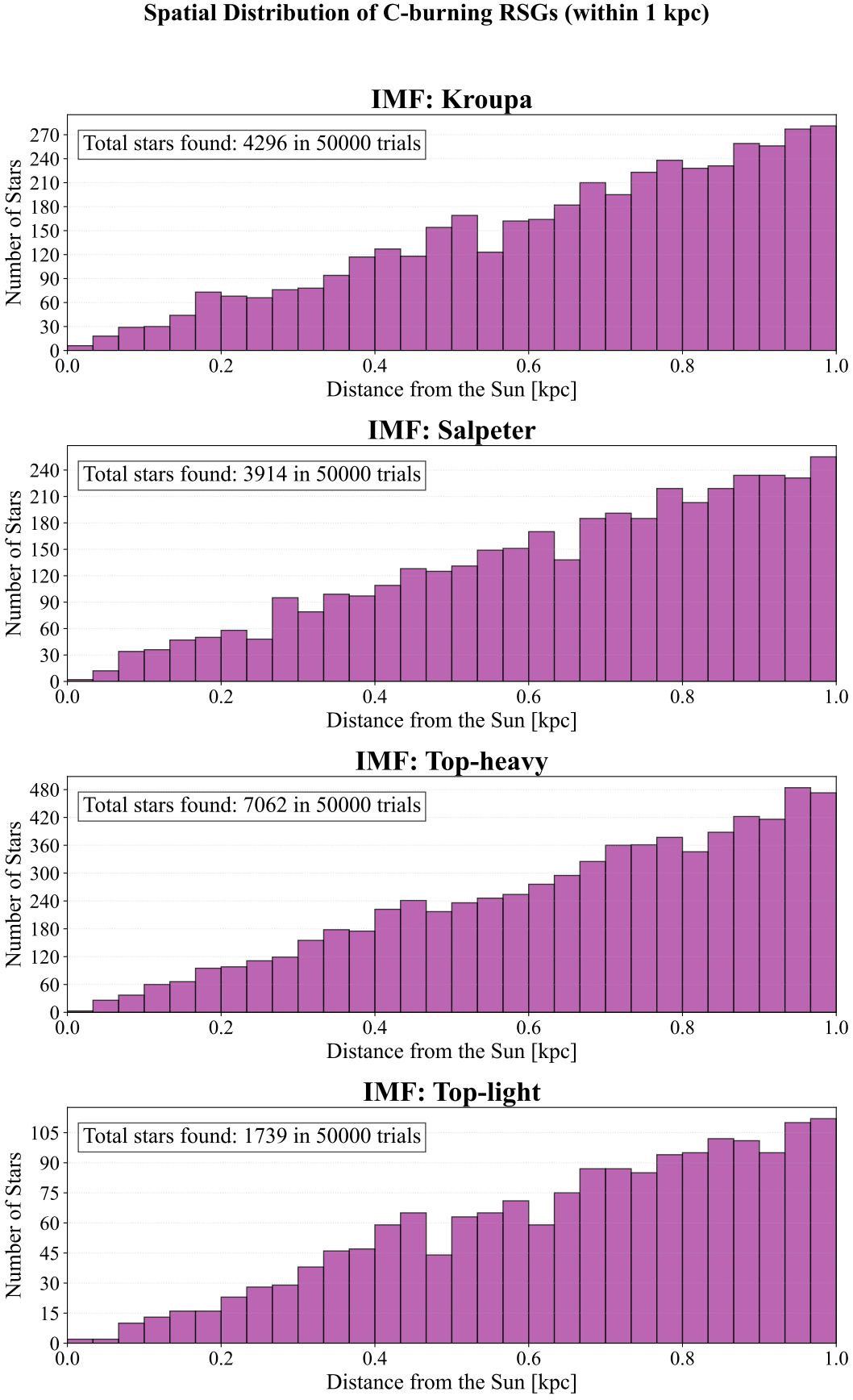

Fig. 2.5: Comparison of the spatial distribution of red supergiants in the carbon-burning phase within a 1 kpc radius from the Sun for different IMF types. The histograms show the number of stars from 50,000 Monte Carlo simulation trials generated with different distances.

2.5.2 Practical calculation of detectability

The practical calculation of the detectability of neutrinos emitted from RSGs in the carbon-burning phase depends on the expected occupancy of stars N_{stars} within a 1 kpc radius. The value of N_{stars} is derived from the different IMF variants using Monte Carlo snapshots. The detectability calculation is performed on differently parameterized detectors with varying masses and different proportions of scintillating liquid in order to obtain a realistic estimate of the potential signal. This represents a simplified toy model for estimation purposes.

The detection of neutrinos depends on their flux, but also on the average neutrino energy E_{avg}, which we introduced as the mean value of the energy spectrum $f(E)$ using the relation 2.11.

$$E_{avg} = \frac{\int_0^{15\text{ MeV}} E \cdot f(E)\, dE}{\int_0^{15\text{ MeV}} f(E)\, dE} \tag{2.11}$$

In the model, the neutrino interaction probability is determined by a linear approximation of the elastic scattering cross-section, where $\sigma(E) \approx 0.9 \times 10^{-44} \cdot E$ cm^2. The elastic scattering cross-section is a value adopted from [15]. The calculation of the total number of target electrons N_e was obtained using a code developed for this work and utilizes Equation 2.12. This value directly affects the interaction cross-section of the detector and, consequently, the probability of detecting neutrinos. For the calculation, we chose the hybrid detector method (WbLS), which combines the advantages of water and an organic scintillator.

The total number of electrons N_e is one of the key parameters for determining the number of interactions. In the case of hybrid detectors, this number is determined by the weighted average of the electron density in both components of the mixture using the relation 2.12. In our implementation, we specifically account for the molar mass and electron count of water (H_2O) and a linear alkylbenzene (LAB) based scintillator.

$$N_e = M_{det} \cdot [(1 - f_{scin}) \cdot n_{e,H_2O} + f_{scin} \cdot n_{e,scin}] \tag{2.12}$$

where M_{det} is the total mass of the detector, f_{scin} represents the mass fraction of the scintillator, and n_e is the electron density (number of electrons per unit mass) for the given component. This procedure allows for a simplified estimation of the electron content within the detector, accounting for the hybrid mixture of water and scintillating solution.

The expected number of detected events per unit of time R is given by the relation 2.13, which utilizes integration over the energy spectrum.

The event rate R is calculated using relation 2.13 and represents an idealized nominal rate before accounting for the realistic response of the detector itself. While the model incorporates the energy-dependent detection efficiency $\eta(E)$ and the energy threshold E_{th}, it does not account for the angular acceptance of the detector or contributions from background processes. This approach is intended to estimate the fundamental physical potential of the hybrid medium

$$R = N_e \cdot \int_{E_{th}}^{15\,\text{MeV}} \Phi_{tot}(E) \cdot \sigma(E) \cdot \eta(E), dE \tag{2.13}$$

Where $\Phi_{tot}(E)$ represents the total differential flux from all stars in the simulated volume. The function $\eta(E)$ defines the detection efficiency, which accounts for the energy threshold E_{th}. Furthermore, $\sigma(E)$ is introduced as a simplified linear approximation, assuming no energy-dependent deviations in the efficiency function above the threshold.

By utilizing hybrid WbLS-based detectors, it is possible to detect low-energy neutrinos with a threshold of $E_{th} = 0.4\,\text{MeV}$. In this model, the efficiency function $\eta(E)$ is defined as a step function: it remains constant at 0.8 for all energies above E_{th} and is zero for all energies below the threshold. This factor is used to account for the detector's sensitivity.

To obtain the most accurate results for neutrino detection, the calculations were performed using two different detector masses: $M_{det} = 20$ kt and $M_{det} = 50$ kt. Furthermore, the volumetric fraction of the scintillation liquid was varied between 5% and 10%. The resulting values presented in Table 3.8 show a comparison between the theoretical number of interactions (N_{raw}) and the expected number of recorded events (N_{exp}), which, for the given detector geometry, is further influenced by the detector efficiency.

To ensure the most accurate processing of the values and to obtain more precise uncertainties, the results from Table 3.8 were averaged by reflecting both the internal variance of the stellar population and the variance among the considered detector configurations. Through this procedure, we sought to achieve a more comprehensive estimate of the actual detectability. The resulting average values with the uncertainties obtained in this manner are listed in Table 3.9.

3 RESULTS AND DISCUSSION

3.1 Variants of the IMF and Their Impact on the Massive Star Population

The variability of the Initial Mass Function (IMF) remains a widely discussed topic; while the slope for low-mass stars is relatively well-established in the literature, significant uncertainty persists for massive stars, which we model in this work using three distinct slope indices defined by α_3. By numerically integrating these three IMF variants over the 12–35 $M_\odot$ mass range, we reveal significant differences in the expected number of massive stars. The results of this comparison are visualized in Figure 3.1, which displays the normalized stellar number density for each scenario.

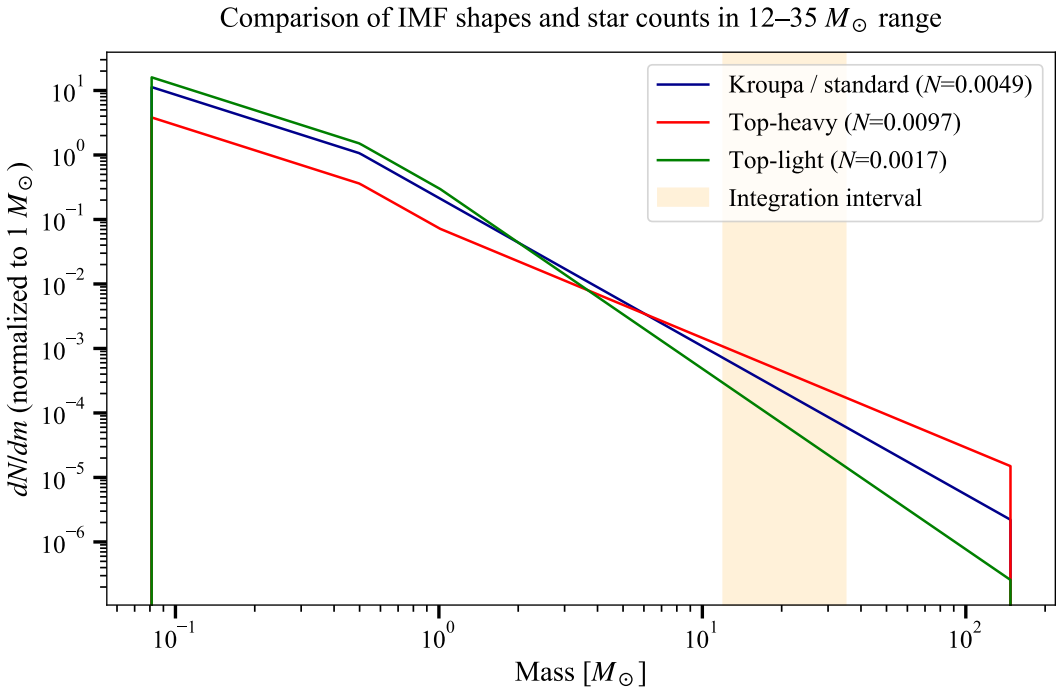

Fig. 3.1: Comparison of three variants of the initial mass function (IMF). The blue curve shows the standard Kroupa IMF ($\alpha_3 = 2.3$); the red curve represents the *top-heavy* variant ($\alpha_3 = 1.7$) with a relatively higher fraction of massive stars; and the green curve depicts the *top-light* variant ($\alpha_3 = 2.8$) with a predominance of low-mass stars. The x-axis gives the stellar mass in units of M⊙, in logarithmic scale, and the y-axis shows the stellar number density dN/dm normalized to a total stellar system mass of 1 M⊙. The orange-shaded region marks the integration interval $12 \leq m/M_\odot \leq 35$, in which the relative number of stars (N) was calculated.

The specific numerical values obtained by integrating the IMF curves within the given mass range are defined in Table 3.1. In this context, N serves as a weighting coefficient expressing the number of stars formed per unit mass of the total population, with each value varying according to the specific slope index α_3 used in the model.

IMF Variant	**Slope index α_3**	**Number of stars N [*per* $M_\odot$]**
Top-heavy	1.7	0.0097
Standard (Kroupa)	2.3	0.0049
Top-light	2.8	0.0017

Tab. 3.1: The number of stars (N) integrated over the 12–35 $M_\odot$ interval for different IMF slope indices α_3. These values represent the numerical yield of massive stars per 1 $M_\odot$ of total formed stellar mass.

The graph compares three initial mass functions (IMFs): the standard Kroupa IMF, the top-heavy IMF, and the top-light IMF. The different slopes of these functions in the high-mass region directly affect the number of massive stars. Integrating these functions over the 12–35 $M_\odot$ mass range gave us the expected number of stars in this mass interval per unit of total stellar mass. The results showed that we obtained $N = 0.0049$ for the standard Kroupa IMF, $N = 0.0097$ for the top-heavy IMF, and $N = 0.0017$ for the top-light IMF. The top-heavy IMF predicts approximately a factor-of-two increase in the number of massive stars compared to the standard model, while the top-light IMF yields a significantly lower count

The variability of the IMF is a topic of debate. While the slope of the function is relatively well-established in the literature for low-mass stars, for massive stars there is a degree of uncertainty, which we model in this work using three different curve slopes defined by α_3. The values below this curve, or

The different values of N — the number of stars per unit mass of the galactic system — illustrate the fundamental role of the slope α_3. While the standard Kroupa value of $\alpha_3 = 2.3$ represents a middle ground, the top-heavy variant with a slope of $\alpha_3 = 1.7$ yields nearly twice the number of massive stars. This slope is often associated with environments of intense star formation or the early universe. In the context of this work, it would also imply the most optimistic prospects for neutrino detection.

In contrast, the top-light model with a slope of $\alpha_3 = 2.8$ represents nearly a third of the number of stars compared to the standard model. This high sensitivity will be reflected in the overall measurements and will affect the differences between values in subsequent steps. Choosing the IMF type is, therefore, a very important step in this regard.

3.2 Stellar Lifetimes and the Carbon-Burning Phase

During the evolution of massive stars, several characteristic thermonuclear reactions occur in the core, with each subsequent stage lasting a shorter time than the previous one. This duration is influenced by several factors, the most significant being the initial mass of the star. To fully understand the detectability of neutrinos, it is necessary to determine the total time span during which a star remains in this specific evolutionary stage.

Stellar lifetimes are heavily dependent on their initial mass. Lower-mass stars have a significantly longer lifetime than more massive ones. According to the calculations, stars with a mass of 12 M⊙ have an approximate lifetime of 17.86 Myr, while stars with a mass of 35 M⊙ reach only 5.45 Myr.

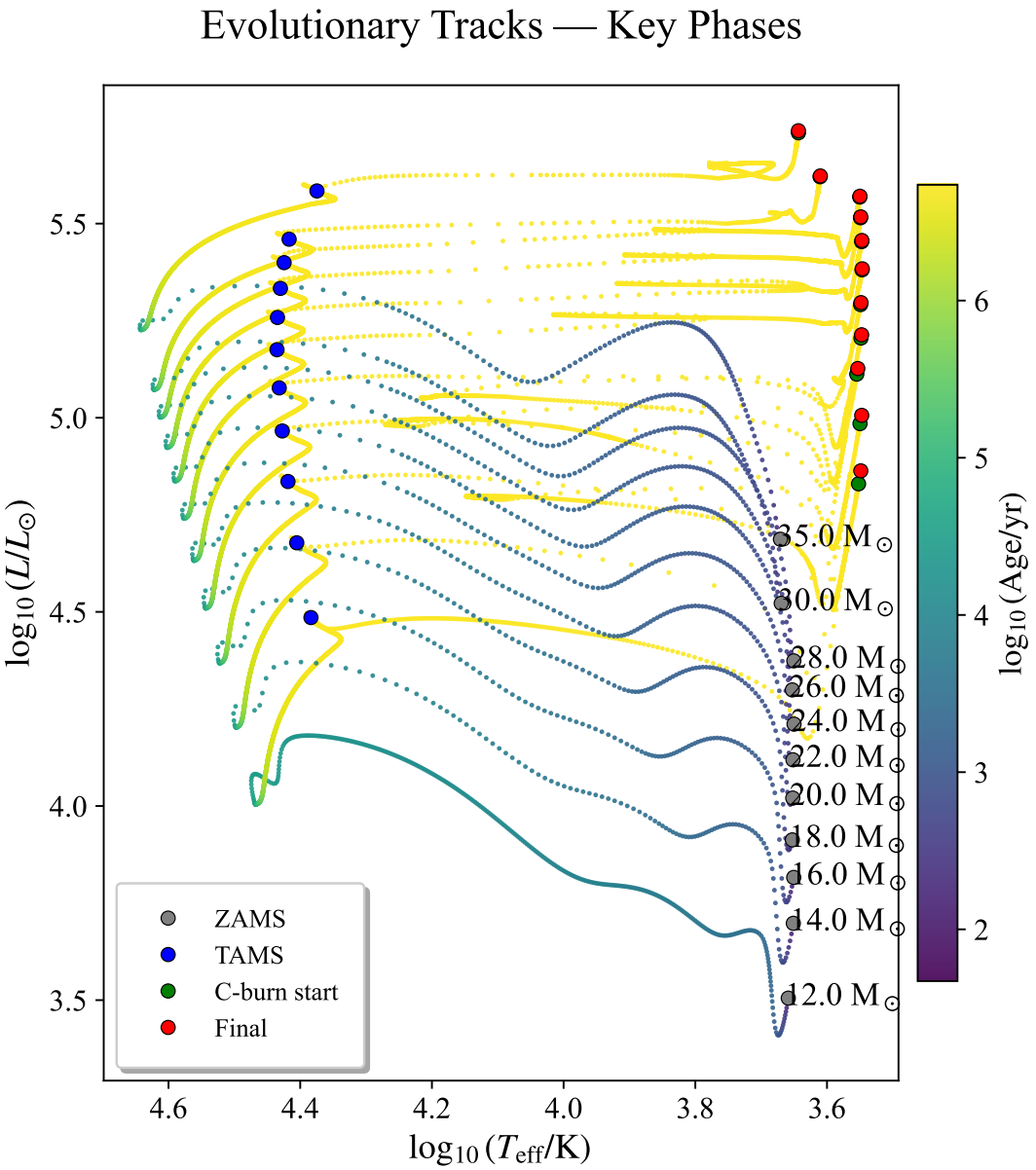

Fig. 3.2: Hertzsprung-Russell diagram for stars with initial masses of 12–35 $M_\odot$. The horizontal axis shows the logarithmic effective temperature and the vertical axis shows the logarithm of luminosity. The color scale represents the logarithmic age of the stars. Key evolutionary stages are marked with colored dots: gray (ZAMS), blue (TAMS), green (beginning of carbon burning), and red (final stage). The onset of the carbon-burning phase (green dots) is numerically identified by a decrease in the central carbon mass fraction of more than 1%; if this criterion cannot be applied, it is subsequently determined by the core temperature reaching $\log_{10}(T_c/{\rm K}) \geq 8.65$.

As shown in Figure 3.2, the evolutionary tracks clearly distinguish the extended hydrogen and helium burning stages from the carbon-burning phase. The green dots represent the onset of carbon ignition, corresponding to the t_{start} values in Table 3.2. The final stage of the simulation is marked by the red dots, represented by t_{end} in the table. This phase, denoted as Δt_C, is significantly shorter and more rapid than the preceding evolutionary stages.

The carbon-burning phase is extremely short compared to the total life of a star. This phase begins later in stars with lower mass than in stars with higher mass. For stars with a mass of 12 M⊙, the phase lasts approximately 8,000 years, while for massive stars of 35 M⊙, it

persists for only about 140 years. Overall, it can be said that as the mass of a star increases, its lifespan shortens, as do the individual phases of its life, such as the duration of advanced nuclear burning. Carbon burning occurs extremely quickly in massive stars, driven by the significantly higher temperatures and pressures within the stellar core.

The specific timing of the onset and conclusion of the carbon-burning stage, along with its total duration (Δt_C) relative to the total stellar lifespan (τ_{total}), is detailed in Table 3.2.

Mass ($M_\odot$)	t_{start} (Myr)	t_{end} (Myr)	Δt_C (Myr)	τ_{total} (Myr)
12.0	17.847460	17.855649	0.008189	17.855516
14.0	14.302001	14.306312	0.004311	14.306093
16.0	11.994703	11.997296	0.002593	11.997106
18.0	10.315532	10.317238	0.001706	10.317067
20.0	9.150593	9.151706	0.001113	9.151562
22.0	8.222779	8.223550	0.000770	8.223427
24.0	7.536243	7.536743	0.000499	7.536638
26.0	6.964542	6.964923	0.000381	6.964832
28.0	6.546990	6.547284	0.000295	6.547204
30.0	6.144511	6.144738	0.000226	6.144677
35.0	5.452610	5.452747	0.000137	5.452700

Tab. 3.2: Timing of the carbon-burning phase for different initial stellar masses.

As shown in Figure 3.2, the evolutionary tracks clearly distinguish the extended hydrogen and helium burning stages from the carbon-burning phase. The green dots represent the onset of carbon ignition, corresponding to the t_{start} values in Table 3.2. The final stage of the simulation is marked by the red dots, represented by t_{end} in the table. This phase, denoted as Δt_C, is significantly shorter and more rapid than the preceding evolutionary stages.

This time span reveals a significant discrepancy in the duration of the carbon-burning phase across different stellar masses. While the most massive stars consume their carbon for only a century and a half, lower-mass stars can remain in this stage for several millennia. Although these less massive stars exhibit lower neutrino luminosity, their higher probability of occurrence makes them more likely candidates for future detection.

When interpreting the final snapshot population, it is important to consider that although lower-mass stars are more numerous in the Milky Way due to the Initial Mass Function and their longer evolutionary lifetimes, the total neutrino signal can be significantly influenced by more massive stars. These are rarer and have shorter carbon-burning phases, but they possess higher core temperatures and thus higher neutrino luminosities.

3.3 Estimation of the Snapshot Population of Carbon-Burning Stars

To determine the number of stars at a given moment—specifically within a particular evolutionary stage—it is necessary to create a detailed snapshot of the galactic population. This calculation takes into account the duration of the specific life stage, the Star Formation Rate (SFR), and the Initial Mass Function (IMF).

The resulting values of the total number of RSGs in the carbon-burning phase, together with their uncertainties, are presented in Table 3.3. This overview allows for a direct comparison of the influence of IMF shapes and the current number of RSGs burning carbon.

IMF	N_{now}	Uncertainty
Kroupa	55	∼7
Top-heavy	92	∼10
Top-light	23	∼5

Tab. 3.3: Estimated snapshot number of carbon-burning stars for different IMF shapes.

The values presented in Table 3.3 are dependent on the Star Formation Rate (SFR) in the Milky Way. It is therefore necessary to note that current estimates of the galactic SFR carry an inherent uncertainty of approximately 20%. Due to the linear scaling of the SFR relative to the snapshot population N_{now}, this uncertainty propagates directly into the final counts and their associated uncertainties. Consequently, while the relative differences between individual IMF models remain constant, the absolute number of stars could vary accordingly.

These figures represent the estimated number of carbon-burning RSGs for the entire galaxy, influenced by several key factors. The choice of the IMF has a significant impact here; the difference between the extremes is as much as sixfold, making the variability of the initial mass function a non-negligible influence on the final count.

These values are strictly dependent on the slope of the IMF and the extremely short duration of the carbon-burning phase relative to the total stellar lifetime. Compared to the enormous total number of stars in the Milky Way, the population of RSGs in this specific stage is limited by the combination of these two factors, resulting in a very small number of observable candidates at any given time.

3.4 Monte-Carlo simulation

The distribution of stars in the Milky Way has a stochastic character, defined by specific probabilities of star formation at different locations. To model this distribution and determine the probability of stars occurring within a given radius, the most effective approach was to employ Monte Carlo methods. By generating numerous possible realizations of the Milky Way's current structure, this simulation allows us to track the statistical distribution of the target stars and determine the most probable outcome.

The Monte Carlo method simulates various possible snapshots of the galactic population. Figure 3.3 illustrates one such realization of a potential stellar distribution. In this figure, red dots represent all RSGs, blue stars represent RSGs in the carbon-burning phase, yellow dots represent stars of other evolutionary types, and gray dots indicate stars that have already died. The figure depicts a snapshot of the current population for the standard Kroupa IMF type.

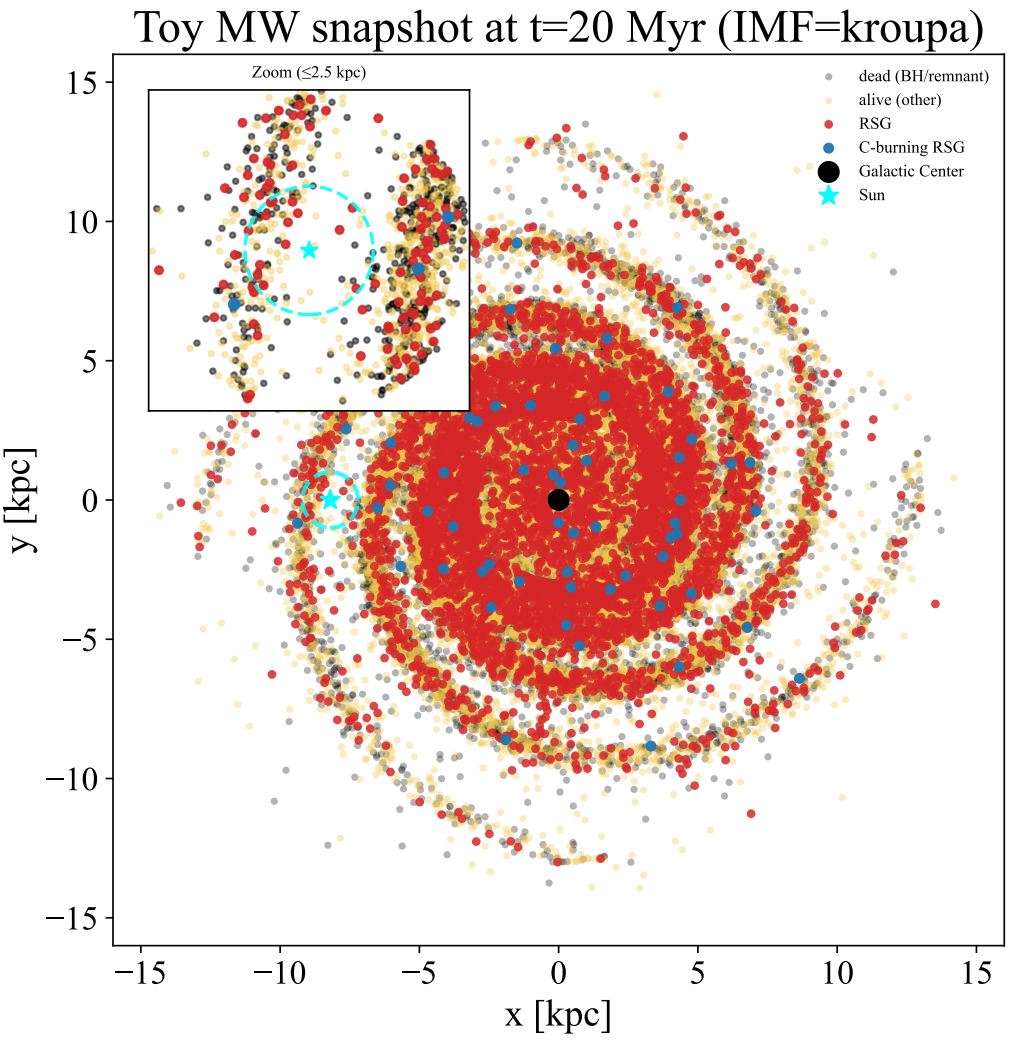

Fig. 3.3: Snapshot of the MW showing the Milky Way as it appears today. Yellow dots represent all alive (other) stars, while gray dots represent dead stars (remnants, BH); red dots represent red supergiants, and blue dots represent RSG stars in the carbon-burning stage. A massive black hole is marked by a black dot at the center. At coordinates $(x, y) = (-8.2, 0)$, our Sun is represented by a turquoise star, surrounded by a circle with a radius of 1 kpc. An inset (close-up) shows our Sun with the 1 kpc circle, providing a more detailed view of the stars within this radius.

The results of the Monte Carlo simulations for quantifying various theoretical models are presented in Table 3.4, showing the total number of RSGs and their distribution within a 1 kpc radius of the Sun. Table 3.5 then lists the population of RSGs specifically in the carbon-burning phase throughout the Milky Way, as well as the expected mean number (λ) of these stars within the 1 kpc radius. According to [15], the probability of an RSG being in the carbon-burning phase is approximately 1%. Our simulation results are consistent with this theoretical expectation, yielding a fraction of 1.1% for stars in the carbon-burning stage relative to the total RSG population.

A key observation from 3.5 is that the expected number of stars within a 1 kpc radius (λ) is less than one across all IMF models. This result must be interpreted as a consequence of stochastic occurrence; therefore, the presence of an RSG in the carbon-burning phase within the solar neighborhood depends more on statistical chance than on the specific IMF slope.

IMF	N_{RSG} (MW)	std	N_{RSG} (<1 kpc)	std
Kroupa	5963	$\pm$ 77	9	$\pm$ 3
Salpeter	5387	$\pm$ 73	8	$\pm$ 2
Top-heavy	10591	$\pm$ 102	16	$\pm$ 4
Top-light	2322	$\pm$ 48	3	$\pm$ 1

Tab. 3.4: Total number of red supergiants (RSGs) in the Milky Way and within 1 kpc of the Sun for different IMFs.

IMF	$N_{\mathrm{C\text{-}RSG}}$ (MW)	std	$\lambda_{\mathrm{C\text{-}RSG}}$ (<1 kpc)	std
Kroupa	55	$\pm$ 7	0.0865	$\pm$ 0.2940
Salpeter	50	$\pm$ 7	0.0783	$\pm$ 0.2793
Top-heavy	92	$\pm$ 9	0.1451	$\pm$ 0.3820
Top-light	22	$\pm$ 4	0.0343	$\pm$ 0.1853

Tab. 3.5: Expected mean number (λ) of RSGs in the carbon-burning phase in the Milky Way and within 1 kpc of the Sun for different IMFs.

The results of the Monte Carlo simulations for individual snapshots vary, and the distribution of the number of RSGs in the C-burning phase is shown in the histograms in Figure 3.4. While the distribution of values for the total number of RSGs in the C-burning phase throughout the MW is quite wide, the number within a one-kpc radius does not show such a wide spread, and in many cases, not a single one of the target stars is found within this radius.

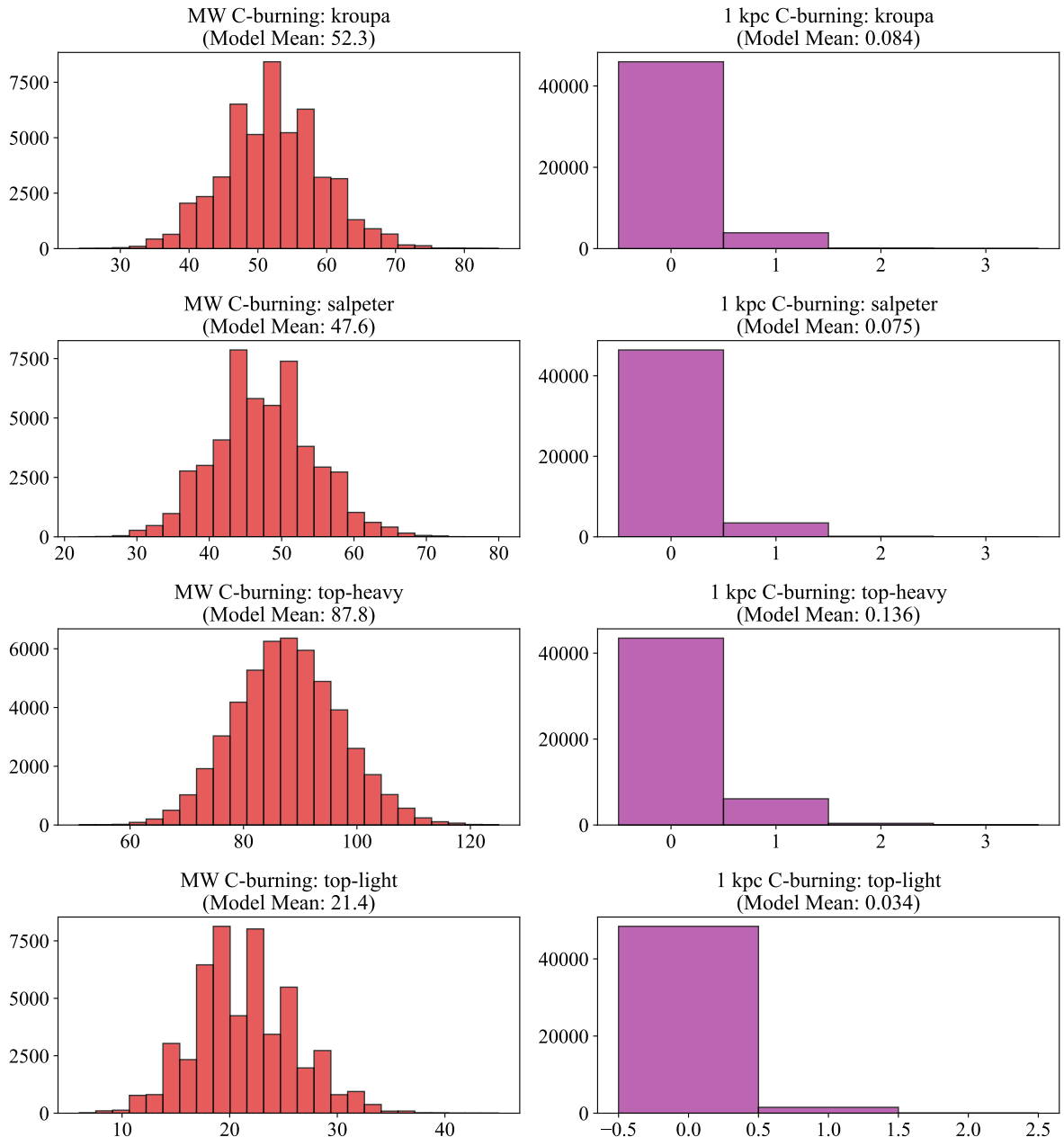

Fig. 3.4: Statistical distribution of carbon-burning red supergiants derived from 50,000 Monte Carlo iterations. The left column (red) shows the total Milky Way population, while the right column (purple) displays the distribution within 1 kpc of the Sun. Results are shown for various IMF models.

Histogram 3.4 illustrates the distribution of C-burning RSGs based on their distance from the Sun for each utilized IMF model. On each graph, the x-axis represents the discrete number of stars predicted by the model within the given volume, while the y-axis shows the frequency of simulation results leading to that specific count. The bars in the histograms represent the frequency of star counts, assuming a Poissonian distribution for the underlying statistics.

A comparison of the total galactic population with the local sample within a 1 kpc radius

highlights a significant statistical challenge. Although red supergiants in the carbon-burning phase occur in relatively large numbers across the entire Milky Way, the local population is extremely sparse, with an improbable occurrence of these stars in our immediate neighborhood. In many Monte Carlo iterations, the total number of stars within 1 kpc was zero, as reflected in the right-hand columns of the histograms in Figure 3.4.

Due to these low counts and high uncertainties, a standard Gaussian summary (mean ± standard deviation) is not physically representative, as it could be interpreted as a negative number of stars. Using the expected mean values, λ, it is possible to determine the actual probability of the occurrence of RSGs in the C-burning phase in our neighborhood. These values are summarized in Table 3.6 for the individual IMF models.

IMF	λ (< 1 kpc)	$P(N = 0)$ [%]	$P(N \geq 1)$ [%]
Kroupa	0.0865	91.71 ± 0.27	8.29 ± 0.27
Salpeter	0.0783	92.47 ± 0.26	7.53 ± 0.26
Top-heavy	0.1451	86.49 ± 0.33	13.51 ± 0.33
Top-light	0.0343	96.63 ± 0.18	3.37 ± 0.18

Tab. 3.6: Probabilities of finding zero, or at least one, carbon-burning RSG within 1 kpc of the Sun.

From an expected value perspective, the results for the Top-heavy IMF are the most favorable, as they provide a 13.51% probability of finding at least one red supergiant in the carbon-burning phase within 1 kpc. In contrast, for the Top-light IMF, the presence of such a red supergiant is nearly improbable, with the probability of no stars of this type occurring within the radius reaching 96.63%. The fact that the uncertainties for these models are several times larger than the mean value itself is direct evidence of the Poissonian nature of rare events.

This statistical rarity suggests that for a neutrino detector, the probability of capturing a neutrino flux from an RSG in the carbon-burning phase is very low. In most snapshots, carbon-burning red supergiants are entirely absent within a 1 kpc radius of the Sun. Even under the most optimistic top-heavy IMF model, the current snapshot of the local population is most likely to be empty. For the standard Kroupa and top-light IMF types, the occurrence of such stars within this radius is nearly improbable. This scarcity strongly limits the possibility of using the neutrino signal as a robust IMF diagnostic. These findings highlight the importance of an expanded detection horizon for identifying these stars, although at greater distances, the neutrino flux becomes weaker and its detection significantly more challenging.

3.5 Neutrino flux from RSG and detection of thermal neutrinos

3.5.1 Neutrino Flux and the Influence of Source Distance

The neutrino flux for an observer from a single star is primarily dependent on its distance. This dependence is shown in Figure 3.5, which presents the estimated values for the neutrino flux from a single red supergiant during the carbon-burning phase. The measured data correspond to a fit using an isotropic emission function $\Phi(r) = L_\nu / 4\pi r^2$, from which we derived a characteristic neutrino luminosity of $L_\nu = 4.79 \times 10^{47}$ s^{-1}.

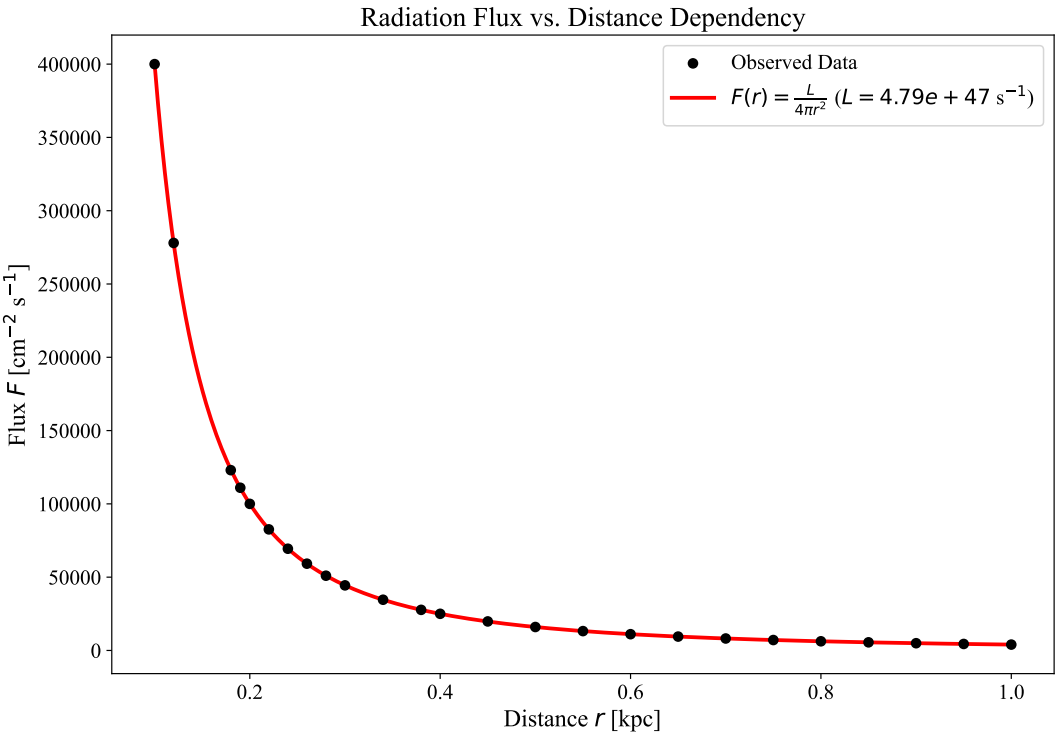

Fig. 3.5: Neutrino flux as a function of distance from a red Supergiant in the carbon-burning phase (RSG). The solid line shows how the number of neutrinos drops with distance, following the physical law of a point source. From our data, we calculated that the star emits approximately 4.79×10^{47} neutrinos every second.

The flux plotted in Figure 3.5 corresponds to a single representative RSG source as a baseline. To determine the expected signal from the integrated local population, this single-source flux is combined with a Monte Carlo simulation of the stochastic distribution of stars within a 1 kpc radius. The model integrates individual contributions by scaling the luminosity of each simulated source according to the inverse-square law relation $\Phi(r) = \frac{L_\nu}{4\pi r^2}$

The total flux from the probabilistic stellar content for different IMF variabilities integrated within a distance of 1 kpc is recorded in Table 3.7.

IMF Model	(N_{stars})	(Φ_{tot}) [cm^{-2}s^{-1}]
Kroupa	0.0873 ± 0.2940	1.55×10^3
Salpeter	0.0775 ± 0.2784	1.38×10^3
Top-heavy	0.1467 ± 0.3820	2.57×10^3
Top-light	0.0357 ± 0.1853	6.43×10^2

Tab. 3.7: Estimated neutrino flux values from red supergiants in the carbon-burning phase within 1 kpc for various IMF models.

The values defined in Table 3.7 are obtained from a simplified theoretical model.

All values correspond to the probabilistic stellar occurrence N_{stars}. The resulting flux is thus correct from a purely mathematical standpoint, but for physical interpretation, a major problem arises when reading the uncertainty for the Top-light model, where values increase extremely when the uncertainty is added. This uncertainty is carried over from the previous Monte Carlo simulation and is caused by the small number of sample stars in the simulation.

3.5.2 Detector Response and Expected Event Rates

Detection is dependent on several detector factors. To ensure the most accurate range of detectability, the theoretical measurement was performed on multiple types of detectors with different criteria. The criteria taken into account are the mass and the percentage occurrence of scintillator liquid in the detector. For all types of IMF variability, calculations were performed on four types of detectors. We varied the mass between a value of 20 kt and a mass of 50 kt. The percentage value of the scintillation liquid was varied between 5% and 10%. The resulting values for individual detectors and individual IMFs are included in Table 3.8.

IMF Model	M_{det} [kt]	**Scint. Fraction** (f_{scin})	N_{exp} [yr^{-1}]
Kroupa	50	10% Scint	3.0544
	50	5% Scint	3.0505
	20	10% Scint	1.2218
	20	5% Scint	1.2202
Salpeter	50	10% Scint	2.7125
	50	5% Scint	2.7090
	20	10% Scint	1.0850
	20	5% Scint	1.0836
Top-heavy	50	10% Scint	5.0569
	50	5% Scint	5.0505
	20	10% Scint	2.0228
	20	5% Scint	2.0202
Top-light	50	10% Scint	1.2635
	50	5% Scint	1.2619
	20	10% Scint	0.5054
	20	5% Scint	0.5048

Tab. 3.8: Estimated total neutrino event rates from Red Supergiants in the carbon-burning phase (within 1 kpc) for different detector configurations. The value N_{exp} reflects the statistical expectation based on the Monte Carlo stellar population and the integrated flux.

It should be noted that the resulting values represent only a theoretical estimate based on an idealized detector model. These figures do not account for complete detector backgrounds or realistic reconstruction efficiencies, which would be present in a real-world experimental setup

For a more precise idea, the calculations from all detection variants were averaged and taken into account within the uncertainties recorded in Table 3.9.

IMF Model	**Average** N_{exp} [**yr**$^{-1}$]
Kroupa	2.137 ± 1.058
Salpeter	1.898 ± 0.940
Top-heavy	3.538 ± 1.749
Top-light	0.884 ± 0.438

Tab. 3.9: Average expected neutrino detection rate for individual IMF models.

Table 3.9 compares the values across different IMF models. These results are purely theoretical; in practice, distinguishing between the individual types of Initial Mass Functions would likely be impossible. Although there is up to a fourfold difference between the extreme values, the uncertainties in these measurements reach nearly 50% of the values themselves. This leads to a significant overlap in the results, making it unfeasible to uniquely distinguish between the individual IMF models based on these observations.

The values used in this model for calculating the neutrino flux and its subsequent detection represent a purely theoretical toy model. For more realistic results, it would be necessary to account for various background sources, which are particularly significant for low-energy thermal neutrinos from an RSG in the carbon-burning phase. Although hybrid WbLS detectors are designed to measure these low-energy neutrinos, the signal-to-background ratio remains a critical factor. Overall, this work outlines the event rates under ideal conditions and provides a basic framework for more complex future simulations.

CONCLUSION

The objective of this thesis was to present a comprehensive theoretical framework for estimating the neutrino flux and detectability of Red Supergiants (RSG) during the carbon-burning phase within the observable neighborhood. Using a custom-built Monte Carlo simulation algorithm, we modeled stellar populations in the Milky Way and compared how different Initial Mass Functions (IMF) affect the expected neutrino flux and subsequent detection of low-energy neutrinos in a toy detector model.

The results of this work demonstrate that the standalone detection of thermal neutrinos from the RSG carbon-burning phase presents a significant observational challenge. While the analysis of population models revealed fundamental differences between individual IMF types—with discrepancies between extreme scenarios reaching a factor of up to 5.7—such detections may contain information about the IMF only under favorable assumptions. Our findings confirm that RSGs in the carbon-burning phase represent approximately 1.1% of the total Red Supergiant population. Ultimately, this approach could theoretically provide a complementary probe in future detector scenarios.

Galaxy simulations using the Monte Carlo method revealed that the expected number of such stars occurring within a 1 kpc radius is less than one in all IMF cases. According to the Poisson distribution, the most optimistic scenario (Top-heavy IMF) gives a 13.51% probability of finding at least one such star. Using an integrated approach to detection rates for hybrid detectors, these simplified calculations suggest that for some IMF models, idealized event rates might reach several detections per year. The Top-heavy model provides the most optimistic scenario, suggesting up to 3.5 detections per year, while the Top-light model shows the lowest detection probability of 0.8 detections per year.It is important to note, however, that these represent idealized event rates before realistic detector-response modelling, background subtraction, and reconstruction efficiency are included.

A key finding of this analysis is that the viability of neutrino-based IMF diagnostics is primarily hindered by the stochastic nature of Red Supergiant occurrence during the carbon-burning phase. Since the probability of finding even a single such source within a 1 kpc radius reaches only 13.51% in the most optimistic scenarios, the practical application of this method is limited by the rarity of local sources rather than the sensitivity of the detector itself. Thus, while the method is theoretically sound, it could provide a complementary probe of the IMF only under favorable assumptions and specific spatial distributions of stars in the solar neighborhood.

A methodological contribution of this work was the verification of neutrino flux scaling. By simulating the flux from individual stellar positions derived from Monte Carlo snapshots for various realizations, we demonstrated the dependence of the signal on the star's distance. We confirmed that accounting for the presence of nearby candidates fundamentally influences the total expected flux and the probabilistic detection.

However, it remains necessary to emphasize that this study worked with a simplified theoretical toy model. In practice, the detection of low-energy thermal neutrinos from RSGs in the carbon-burning phase will face a severe background problem, which is reflected in the high variance of our results where uncertainties are comparable to the mean values. Nevertheless, the development of hybrid detector technology (WbLS) could, thanks to future advancements, offer a way to distinguish the signal from solar neutrinos and antineutrinos from terrestrial reactors by combining Cherenkov radiation and scintillation fluid measurements.

Although the statistical probability of capturing a neutrino signal from an RSG in the burning phase is low, this work provides a necessary statistical foundation for future, more complex simulations that will include realistic detection background models, a more detailed structure of the Galaxy, and stellar evolution.

The presented work offers scope for future research in several directions. A fundamental step is the implementation of a realistic detector background model, which will allow for a more

accurate determination of the signal-to-noise ratio and the actual sensitivity of the instruments. Further refinement of the model should include sensitivity to a wider range of RSG masses and the influence of binary systems or mass loss on stellar evolution. These factors can significantly modify the duration of the carbon-burning phase as well as the resulting neutrino luminosity. To verify the theoretical results, a comparison of simulations with real observational data and galactic RSG catalogues will be essential in the future. Furthermore, it would be crucial to test the influence of various spatial distributions of stellar mass within the galactic disk to better quantify the probability of detecting these rare evolutionary phases.

Bibliography

[1] Edwin E. Salpeter. The Luminosity Function and Stellar Evolution. *The Astrophysical Journal*, 121:161, January 1955. doi:10.1086/145971.

[2] Pavel Kroupa. On the variation of the initial mass function. *Monthly Notices of the Royal Astronomical Society*, 322(2):231–246, 2001. doi:10.1046/j.1365-8711.2001.04022.x.

[3] Gilles Chabrier. Galactic stellar and substellar initial mass function. *Publications of the Astronomical Society of the Pacific*, 115(809):763–795, 2003. doi:10.1086/376392.

[4] Andrew M. Hopkins. The dawes review 8: Measuring the stellar initial mass function. *Publications of the Astronomical Society of Australia*, 35:e039, 2018. arXiv:1807.09949, doi:10.1017/pasa.2018.29.

[5] Tereza Jerabkova et al. Cosmic threads: Interlinking the stellar initial mass function from star-birth to galaxies. *arXiv e-prints*, page arXiv:2509.06886, 2025. arXiv:2509.06886, doi:10.48550/arXiv.2509.06886.

[6] Pavel Kroupa. The Initial Mass Function of Stars: Evidence for Uniformity in Variable Systems. *Science*, 295(5552):82–91, January 2002. arXiv:astro-ph/0201098, doi:10.1126/science.1067524.

[7] Gwangeon Seong, Kyujin Kwak, Dongsu Ryu, and Bok-Kyun Shin. Neutrinos from carbon-burning red supergiants and their detectability. *arXiv e-prints*, page arXiv:2502.05404, 2025. arXiv:2502.05404, doi:10.48550/arXiv.2502.05404.

[8] K. Abe et al. Hyper-kamiokande design report. *arXiv e-prints*, page arXiv:1805.04163, 2018. arXiv:1805.04163, doi:10.48550/arXiv.1805.04163.

[9] Fengpeng An et al. Neutrino physics with juno. *Journal of Physics G: Nuclear and Particle Physics*, 43(3):030401, 2016. arXiv:1507.05613, doi:10.1088/0954-3899/43/3/030401.

[10] John F. Beacom and Mark R. Vagins. Gadzooks! antineutrino spectroscopy with large water cherenkov detectors. *Physical Review Letters*, 93(17):171101, 2004. arXiv:hep-ph/0309300, doi:10.1103/PhysRevLett.93.171101.

[11] Pavel Kroupa, Eda Gjergo, Tereza Jerabkova, and Zhiqiang Yan. The initial mass function of stars, 2024. URL: https://arxiv.org/abs/2410.07311, arXiv:2410.07311.

[12] Richard B. Larson. Thermal physics, cloud geometry and the stellar initial mass function. *MNRAS*, 359(1):211–222, May 2005. arXiv:astro-ph/0412357, doi:10.1111/j.1365-2966.2005.08881.x.

[13] Jiadong Li, Chao Liu, Zhi-Yu Zhang, Hao Tian, Xiaoting Fu, Jiao Li, et al. Stellar initial mass function varies with metallicity and time. *Nature*, 613(7944):460–462, 2023. doi:10.1038/s41586-022-05488-1.

[14] Richard B. Larson. Early star formation and the evolution of the stellar initial mass function in galaxies. *Monthly Notices of the Royal Astronomical Society*, 301(2):569–581, December 1998. arXiv:astro-ph/9808145, doi:10.1046/j.1365-8711.1998.02045.x.

[15] Gwangeon Seong, Kyujin Kwak, Dongsu Ryu, and Bok-Kyun Shin. Neutrinos from carbon-burning red supergiants and their detectability, 2025. URL: https://arxiv.org/abs/2502.05404, arXiv:2502.05404.

[16] Sylvia Ekström and Cyril Georgy. Stellar evolution through the red supergiant phase. *Galaxies*, 13(4):81, jul 2025. URL: http://dx.doi.org/10.3390/galaxies13040081, doi:10.3390/galaxies13040081.

[17] Schuyler D. Van Dyk. Red supergiants as supernova progenitors, 2025. URL: https://arxiv.org/abs/2507.15973, arXiv:2507.15973.

[18] Po-Sheng Ou and Ke-Jung Chen. Why Do Stars Turn Red? II. Steady-State Envelope Solutions. *arXiv e-prints*, page arXiv:2506.07630, June 2025. arXiv:2506.07630, doi:10.48550/arXiv.2506.07630.

[19] Emily M. Levesque. The physical properties of red supergiants, 2009. URL: https://arxiv.org/abs/0911.4720, arXiv:0911.4720.

[20] Roberta M. Humphreys. Red supergiants—the other side of the h-r diagram. *Galaxies*, 13(2):25, mar 2025. URL: http://dx.doi.org/10.3390/galaxies13020025, doi:10.3390/galaxies13020025.

[21] Tuguldur Sukhbold and Scott Adams. Missing red supergiants and carbon burning. *Monthly Notices of the Royal Astronomical Society*, 492(2):2578–2587, jan 2020. URL: http://dx.doi.org/10.1093/mnras/staa059, doi:10.1093/mnras/staa059.

[22] Chinami Kato, Hiroki Nagakura, Shun Furusawa, Koh Takahashi, Hideyuki Umeda, Takashi Yoshida, Koji Ishidoshiro, and Shoichi Yamada. Neutrino emissions in all flavors up to the pre-bounce of massive stars and the possibility of their detections. *The Astrophysical Journal*, 848(1):48, 2017. arXiv:1704.05480, doi:10.3847/1538-4357/aa8b72.

[23] Andrzej Odrzywołek, Mirosław Misiaszek, and Marek Kutschera. Detection possibility of the pair-neutrino emission from the neutrino-cooled pre-supernova star. *Astroparticle Physics*, 21(3):303–313, 2004. doi:10.1016/j.astropartphys.2004.02.002.

[24] K. Asakura et al. Kamland sensitivity to neutrinos from pre-supernova stars. *The Astrophysical Journal*, 818(1):91, 2016. arXiv:1506.01175, doi:10.3847/0004-637X/818/1/91.

[25] S. J. Smartt, J. J. Eldridge, R. M. Crockett, and J. R. Maund. The death of massive stars - i. observational constraints on the progenitors of type ii-p supernovae. *Monthly Notices of the Royal Astronomical Society*, 395(3):1409–1437, May 2009. URL: http://dx.doi.org/10.1111/j.1365-2966.2009.14506.x, doi:10.1111/j.1365-2966.2009.14506.x.

[26] J. Caravaca, B. J. Land, M. Yeh, and G. D. Orebi Gann. Characterization of water-based liquid scintillator for cherenkov and scintillation separation. *The European Physical Journal C*, 80(9), September 2020. URL: http://dx.doi.org/10.1140/epjc/s10052-020-8418-4, doi:10.1140/epjc/s10052-020-8418-4.

[27] A.V. Lyashenko, B.W. Adams, M. Aviles, T. Cremer, C.D. Ertley, M.R. Foley, M.J. Minot, M.A. Popecki, M.E. Stochaj, W.A. Worstell, J.W. Elam, A.U. Mane, O.H. W. Siegmund, H.J. Frisch, A.L. Elagin, E. Angelico, and E. Spieglan. Performance of large area picosecond photo-detectors (lappdtm). *Nuclear Instruments and Methods in Physics Research Section A: Accelerators, Spectrometers, Detectors and Associated Equipment*, 958, 2020. URL: http://dx.doi.org/10.1016/j.nima.2019.162834, doi:10.1016/j.nima.2019.162834.

[28] Mohan Li, Ziyi Guo, Minfang Yeh, Zhe Wang, and Shaomin Chen. Separation of scintillation and cherenkov lights in linear alkyl benzene. *Nuclear Instruments and Methods in Physics Research Section A: Accelerators, Spectrometers, Detectors and Associated Equipment*, 830:303–308, September 2016. URL: http://dx.doi.org/10.1016/j.nima.2016.05.132, doi:10.1016/j.nima.2016.05.132.

[29] Steven D. Biller, Edward J. Leming, and Josephine L. Paton. Slow fluors for effective separation of cherenkov light in liquid scintillators. *Nuclear Instruments and Methods in Physics Research Section A: Accelerators, Spectrometers, Detectors and Associated Equipment*, 972:164106, aug 2020. URL: http://dx.doi.org/10.1016/j.nima.2020.164106, doi:10.1016/j.nima.2020.164106.

[30] PARSEC Team. Parsec v2.0: Stellar tracks of intermediate to very massive stars, 2026. Online database, accessed 3 March 2026. URL: https://stev.oapd.inaf.it/PARSEC/tracks_v2_VMS.html.

[31] Alessandro Bressan, Paola Marigo, Léo Girardi, Bernardo Salasnich, Cristiana Dal Cero, Stefano Rubele, and Ambra Nanni. Parsec: stellar tracks and isochrones with the padova and trieste stellar evolution code. *Monthly Notices of the Royal Astronomical Society*, 427(1):127–145, 2012. arXiv:1208.4498, doi:10.1111/j.1365-2966.2012.21948.x.

[32] Laura Chomiuk and Matthew S. Povich. Toward a unification of star formation rate determinations in the milky way and other galaxies. *The Astronomical Journal*, 142(6):197, 2011. arXiv:1110.0220, doi:10.1088/0004-6256/142/6/197.

[33] L. G. Hou and J. L. Han. The observed spiral structure of the milky way. *Astronomy & Astrophysics*, 569:A125, 2014. doi:10.1051/0004-6361/201424039.

[34] M. J. Reid, K. M. Menten, A. Brunthaler, X. W. Zheng, T. M. Dame, Y. Xu, Y. Wu, B. Zhang, A. Sanna, M. Sato, K. Hachisuka, Y. K. Choi, K. Immer, L. Moscadelli, K. L. J. Rygl, and A. Bartkiewicz. Trigonometric parallaxes of high-mass star-forming regions: Our view of the milky way. *The Astrophysical Journal*, 885:131, 2019. doi:10.3847/1538-4357/ab4a11.

[35] V. V. Bobylev and A. T. Bajkova. Milky way spiral structure parameters from data on masers and selected open clusters. *Monthly Notices of the Royal Astronomical Society*, 437:1549–1559, 2014. doi:10.1093/mnras/stt1987.

[36] J. P. Vallée. Different studies of the global pitch angle of the milky way's spiral arms. *Monthly Notices of the Royal Astronomical Society*, 450:4277–4284, 2015. doi:10.1093/mnras/stv882.

[37] M. J. Reid, K. M. Menten, A. Brunthaler, X. W. Zheng, T. M. Dame, Y. Xu, Y. Wu, B. Zhang, A. Sanna, M. Sato, K. Hachisuka, Y. K. Choi, K. Immer, L. Moscadelli, K. L. J. Rygl, and A. Bartkiewicz. Trigonometric parallaxes of high mass star forming regions: The structure and kinematics of the milky way. *The Astrophysical Journal*, 783:130, 2014. doi:10.1088/0004-637X/783/2/130.

[38] J. P. Vallée. The spiral arms of the milky way: The relative location of each different arm tracer, within a typical spiral arm width. *The Astronomical Journal*, 148:5, 2014. doi:10.1088/0004-6256/148/1/5.

Symbols and abbreviations

RSG	Red supergiant
MW	Milky Way
IMF	Initial Mass Function
UV	Ultraviolet (radiation)
SFR	Star Formation Rate
ZAMS	Zero-Age Main Sequence
TAMS	Terminal-Age Main Sequence
HRD	Hertzsprung–Russell diagram
std	standard deviation
$M_\odot$	Solar mass
$L_\odot$	Solar luminosity
$R_\odot$	Solar radius
MS	Main Sequence
IBD	Inverse Beta Decay
WbLS	Water-based Liquid Scintillator
LAPPD	Large Area Picosecond Photodetector
JUNO	Jiangmen Underground Neutrino Observatory
HK	Hyper-Kamiokande
PMT	Photomultiplier Tube
CNO	Carbon-Nitrogen-Oxygen (cycle)
MeV	Megaelectronvolt
Myr	Million years
MC	Monte Carlo (simulation)
kpc	Kiloparsec

List of appendices

A Code Repository

A.1 RSG C-burning Phase Analysis

The analysis of the Red Supergiant (RSG) carbon-burning phase was performed using the code stored in the following repository:

- **Repository URL:** https://github.com/klarasvestkova4444/RSG-C-burning-phase
- **Directory/Branch:** `main`
- **Description:** This repository contains individual Python code snippets used for the theoretical calculation of RSG during the carbon burning phase in MW for various types of IMFs.

Execution Procedure

1. **Requirements:** Python 3.x with `numpy`, `matplotlib`, and `scipy` libraries installed.
2. **Running the Code:** Open the desired script in a Python IDE (e.g., VS Code) and execute it using the **Run** command.
3. **Output:** Numerical data is output to the console, and visualizations are rendered in interactive `matplotlib` windows via the `plt.show()` command.

Code Structure and Description and Data collected and used in the study

1. `HR diagram.py` - Calculation of individual stellar evolution phases and lifetimes, corresponding to the analysis in Chapter 2.2.
2. `IMF kroupa vz salpeter.py` - Graphical comparison of the Salpeter and Kroupa initial mass functions as presented in Figure 1.1.
3. `integration IMF.py` - Computation of integration curves for various IMF models shown in Figure 3.1.
4. `mathematical model MW.py` - Mathematical representation and geometric modeling of the Milky Way, described in Chapter 2.4.3.
5. `neutrino flux.py` - Calculation of the relationship between source distance and neutrino flux, visualized in Figure 3.5.

A.2 Monte Carlo Simulation

The Monte Carlo analysis was performed using code stored in the following repository

- **Repository URL:** https://github.com/klarasvestkova4444/neutrino_project
- **Directory/Branch:** `main`
- **Description:** This repository contains a toy model written in Python that calculates the number of stars using a Monte Carlo simulation.

The fastest way to run (recommended)

1. Open `run_pipeline.py` and adjust the `CONFIG` block if specific parameters need to be modified.
2. Run the main script from the terminal:

```
python3 run_pipeline.py
```

Data collected and used in the study

- **Figure 3.3:** Generated from the output file `outputs/mw_snapshot_map.png`.
- **IMF Analysis** Data extracted from `outputs/imf_scan.csv`.Data on the calculation of the number of stars in the Milky Way and the probability of a supermassive black hole within 1 kpc for the chapter 3.4